AIMS Mathematics, 11(6): 18361–18401.
DOI: 10.3934/math.2026746
Received: 30 July 2025
Revised: 22 September 2025
Accepted: 26 September 2025
Published: 22 June 2026

https://www.aimspress.com/journal/Math

Research article

Enhancing stability and reliability of renewable-powered DC microgrids using integral backstepping control with nonlinear observers and load uncertainty consideration

Hassan Abouobaida[1], Safeer Ullah[2], Muhammad Zeeshan Babar[3,*], Sultan Alghamdi[4] and Ahmed S. Alsafran[5]

[1] Advanced Systems Engineering Laboratory, National School of Applied Sciences, Ibn Tofail University, Kénitra, Morocco
[2] Department of Electrical Engineering, Quaid-e-Azam College of Engineering and Technology, Sahiwal 57000, Pakistan
[3] School of Engineering and Physical Sciences, Heriot-Watt University, Edinburgh EH14 4AS, United Kingdom
[4] Center of Research Excellence in Renewable Energy and Power Systems, Department of Electrical and Computer Engineering, King Abdulaziz University, Jeddah 21589, Saudi Arabia
[5] Department of Electrical Engineering, College of Engineering, King Faisal University, Al Ahsa 31982, Saudi Arabia

* **Correspondence:** Email: m.babar@hw.ac.uk; Tel: +44-7888263527.

Abstract: This study presented an integral backstepping (IB) controller to enhance the dynamic stability of direct current (DC) microgrids by effectively managing their interconnected components. The proposed control strategy generated switching signals for power converters, enabling seamless coordination among solar photovoltaic (PV) generators, wind generators, and battery energy storage systems with the common DC bus. By ensuring the convergence of all state variables to their desired values, the controller guaranteed system stability, which was rigorously analyzed using Lyapunov theory. To further optimize performance, state observers were employed to monitor DC microgrid currents, power flows, and load disturbances, improving sensor accuracy, reducing costs, and enhancing system reliability. Comprehensive simulations validated the controller's effectiveness in maintaining power balance under varying operating conditions. Compared to conventional methods,

the proposed approach significantly improved the DC bus voltage regulation and overall dynamic performance of the microgrid.

Keywords: DC microgrids; integral backstepping control; nonlinear observers; photovoltaic (PV) systems; wind energy systems; battery energy storage; power converter control; sensor reduction
Mathematics Subject Classification: 49N90, 93C10

1. Introduction

Microgrids are a sophisticated technique under modern power systems, which form a mainstay for allowing distributed energy resources (DERs) to operate in a synchronized manner, thus ensuring a stable, sustainable, and reliable power supply. They help improve energy security, transmission loss reduction, as well as facilitate easy assimilation of renewable power. Microgrids promote worldwide energy sustainability by being able to operate independently of the main grid in regions with substandard or non-existent power infrastructure. They support local generation, transmission, distribution, and storage of electricity, which makes them a means for local economic development while mitigating environmental impacts from traditional hydrocarbon burning [1,2].

Microgrids can be divided into three types: alternating current (AC), direct current (DC), and an AC-DC combination known as the hybrid microgrid. A microgrid based on AC must be able to interwork with the traditional grid. DC microgrids continue to be preferred for DC-based DERs like solar and battery storage solutions, as they provide a more cost-effective integration that serves loads by eliminating the power conversion to AC in most of the building-mounted appliances [3,4]. Hybrid microgrids: Hybridization of AC and DC systems leads to better results and higher flexibility [5,6]. The microgrids of all types have features and applications driven by particular operational requirements and the availability of resources. DC microgrids have a few attractive features that are different from AC ones, such as efficiency and the integration of renewable energy [7]. Since the majority of DERs are DC when they are generated natively, energy conversions have to stay partially obsolescent with DC microgrids by nipping in the bud or by wholly getting rid of a certain number of inefficient operations and, as a result, improving system efficiency. In addition, DC microgrids can more readily interface with standard electronic devices on the downstream side, including power conversion and energy storage devices, which frequently eliminates the requirement to convert to AC [8]. It helps achieve a simple system level organization that can be more reliable and less costly to maintain. The DC microgrids are an essential part of the next generation power systems [9] as a result of growing attention towards sustainability and renewable energy.

Scaling up wind and solar manufacturing capacity also makes microgrids more sustainable and cost-effective. Solar and wind power are environmentally friendly with a low cost of production [10]. Enhanced production, thus, enables microgrids to decrease dependency on fossil fuels and greenhouse gases and increase power security [11]. The efficient utilization of wind and solar energy promotes the development of the low-carbon economy, which is consistent with the world climate goals. The expansion of renewable power generation may also serve to boost the economy through lowering power costs and providing new employment opportunities in the renewable power field [12].

To boost the efficiency of PV and wind power systems, maximum power point tracking (MPPT) algorithms play a central role in optimizing performance under varying conditions. There are numerous

MPPT methods, each with characteristic features and applications. Advanced MPPT algorithms are essential for boosting renewable energy output, such as PV power, as well as wind power output. Researchers in [13] presented a non-isolated high step-up DC-DC converter designed for a solar PV-centric DC microgrid, which offers a high-voltage conversion magnitude alongside smaller component size, with high efficiency, comprising a modified perturb and observe (P&O) control algorithm for MPPT, which was validated via simulation results as well as experimental results. While the P&O technique remains simple for users, with a simple control design, its performance suffers under rapidly changing conditions [14]. In contrast, incremental conductance (INC) techniques offer improved accuracy and faster response with increased complexity [15]. An artificial neural network (ANN)-oriented INC supervisory control technique for PV power under microgrid conditions was presented in [16] by integrating constant power (CP) mode with MPPT mode for stabilizing power generation under changing environmental conditions, with a view to ensuring precise power regulation as well as seamless operation with minimal oscillations as well as rapid dynamics, as validated via MATLAB Simulink simulation results. While fuzzy logic-based MPPT algorithms exhibit applicability for a variety of scenarios, they require extensive adaptation [17]. A fuzzy logic controller (FLC)-centric MPPT technique was presented in [18] for a DC microgrid fed by solar PV as well as fuel cell power, for optimizing efficiency under varied conditions of irradiance as well as temperatures via rapid adaptation to the environment for enhancing system reliability, as well as an increased FLC design concept for a DC-DC boost converter. Hybrid MPPT controllers, which integrate techniques such as P&O, INC, or fuzzy logic, showed remarkable performance enhancements as they react promptly to rapid dynamical changes in irradiance [19]. It allows, therefore, that a PV system, as well as a wind system, in a microgrid operation, work under its maximum power point (MPP), translating to an overall improved efficiency of a specified stand-alone or part-of-islanded microgrid. [20] described a PV-based microgrid system with grid connection via an H-bridge voltage-source inverter having a hybrid controller for optimizing its performance, which employed an INC MPPT for maximum power extraction and a sliding-mode control (SMC) for improving power quality, having a faster response, lower harmonics, and increased robustness, as contrasted with a proportional integral (PI) +proportional integral derivative (PID) hybrid controller. Other new approaches, such as neural networks, particle swarm optimization, or others, are also extremely efficient, but they require more computational power [21,22]. Both algorithms entail compromises, with a decision based on individual application needs as well as system characteristics. A hybrid particle swarm-optimization/grey wolf-optimizer algorithm was suggested in [23] as a control algorithm for DC microgrids in its local control layer for improving system problems such as imprecise power-sharing, unchecked DC-bus-voltage, excessive battery-current-ripple, with notable improvements in power distribution between PV, battery, and supercapacitor technologies, with minimized settling time as well as overshoot/undershoot with changing loads as well as generation conditions.

The selection of control strategies is crucial for stable, reliable, and efficient microgrid operations. Although linear control systems have the advantages of a relatively simple design and common usage in various applications, they may not exhibit effective behavior under nonlinear and dynamic conditions accompanying microgrids [24]. Nonlinear control strategies, such as SMC [25] and backstepping control [26], have been used to tackle these issues because of their robustness and good performance under different operating conditions. A double integral SMC was proposed in [27] for PV converters in DC microgrids to ensure smooth and seamless transitions between MPPT and constant voltage control modes by controlling the PV converter as a voltage source in both modes, as

demonstrated through simulations and experimental tests. SMC is a disturbance- and uncertainty-robust method, but it has a chattering effect with specific inputs. In contrast, backstepping is a nonlinear control technique that has been widely used to derive controllers for certain classes of nonlinear systems, offering the high precision and robustness required in microgrid applications [28]. Backstepping control has been considered as a systematic approach to design controllers, and it is widely used for the exact regulation problem of nonlinear systems, especially in the complete regulation sense for coupling terms inherent within periodic variations of microgrid dynamical equations. More recently, advanced integral-backstepping (IB) enhancements have been proposed, such as the adaptive nonlinear IB with double deep Q-learning for frequency stabilization in cyber-physical shipboard microgrids [29], and the continuous reactive power regulation strategy for hybrid high-voltage direct current (HVDC) transmission systems [30]. While these contributions demonstrate significant progress, their focus is on maritime systems or large-scale HVDC networks, and thus they do not directly address the challenges of voltage regulation and disturbance rejection in renewable-powered DC microgrids. IB remains particularly promising for such applications, as it integrates integral action to eliminate steady-state errors and improve dynamic performance [28]. The adoption of backstepping and IB controls represents a significant advancement in modern MPPT techniques for DC microgrid optimization [31], ensuring that PV and wind systems consistently operate at their MPP while maintaining overall system reliability and sustainability. These control techniques ensure that PV and wind systems in microgrid operations consistently operate at their MPP, thereby boosting the overall efficiency and sustainability of the microgrid. It should be noted that even for general linear observers, such as the Luenberger observer, which are quite easy to design and simpler to implement, they perform reasonably well in many situations when compared with other higher-order observers [32]. However, they do not perform well in nonlinear scenarios. To deal with nonlinearities, observers such as the extended Kalman filter (EKF) [33] and sliding mode observers [27] have been proposed for precise estimates of states under different operating conditions. Researchers in [34] addressed the challenges of actuator fault estimation, state estimation, and bus voltage control in DC microgrids with linear and nonlinear constant power loads, proposing a dual-extended Kalman filter (dual-EKF) for fault and state estimation, and a linear parameter varying model predictive control for regulating current and voltage, offering robust, adaptive control with reduced computational burden, and validated by numerical simulations.

Microgrids are nonlinear systems by nature; thus, proper state estimation is required by employing well-suited observers. For modern microgrid control strategies, nonlinear observers such as the extended high-gain observer (EHGO) [35] and nonlinear disturbance observer (NDO) [36] are used. EHGOs are highly efficient tools for the online state estimation of plant systems; they have high accuracy and fast-converging properties that enable them to be used in real-time control applications. NDOs are designed to forecast failures and system behavior and are operational correctly even in the presence of abnormal configurations [36]. Because of their precision and fast convergence, they can be deployed in real-time settings (low latency) when a high level of accuracy in state estimation is required [37]. For the stability and security of microgrids, especially in predictive disturbance cases, it is important that their operational performance is reliable. These observations improve the performance and trustworthiness of their most efficient. By wisely integrating them in DC microgrids, it could disrupt the path to the next occurrence of advanced and environmentally friendly control loops, with leading prospects for sustainable reliable systems.

Most recent studies on nonlinear control approaches have shown considerable advances beyond classical methods. Adaptive neural network (NN) observer-based synthesis techniques, for instance, have been employed to address uncertainties inherent in nonlinear renewable energy systems, improving adaptability as well as boosting robustness [38–40]. It has been demonstrated that neural Lyapunov methods can be combined with traditional Lyapunov approaches for efficient and accurate stability analysis of uncertain nonlinear systems. Furthermore, neural controllers with fractional-order analysis of stability were shown to possess adequate ability to control the complexity of microgrid dynamics, subsequently ensuring improved assurances on performance under conditions that are uncertain as well as time-variant. Such studies reflect an emerging trend toward intelligent, adaptive, as well as computationally efficient nonlinear control designs for application in renewable energy integration. On this basis, our proposed framework implements an IB methodology that comprehensively addresses issues related to steady-state regulation, while applying nonlinear observers for purposes of estimation that are robust, closing an existing gap in literature.

Although the limitations of DC microgrids have been widely studied, several challenges remain. A key issue lies in integrating nonlinear control and estimation within a unified framework to handle their nonstationary and uncertain behavior. Furthermore, research on developing efficient and adaptive MPPT algorithms compatible with advanced management strategies is still ongoing. To the best of the authors' knowledge, this work is the first to propose a simple integrated control and observation technique for a nonlinear DC–DC converter in a DC microgrid using an IB-based approach, enhancing both MPPT performance and overall system stability.

The contributions of this study are summarized as follows:

- The proposed control framework adopts an IB approach that mitigates steady-state errors through integral action, ensuring higher precision and stability in DC microgrid operations.
- The incorporation of the P&O MPPT algorithm enhances the performance of renewable energy generation, optimizing the microgrid's power output.
- Nonlinear observers are employed for accurate state estimation and disturbance rejection, improving the reliability of the control system.
- The effectiveness of the proposed framework is validated under diverse simulation scenarios, demonstrating its robustness and adaptability.
- A key innovation of this paper lies in the integration of IB with nonlinear observers and explicit handling of load uncertainty, which is not jointly addressed in prior work.

In a nutshell, this work highlights the indispensable role of DC bus voltage regulation for power balance and microgrid stability. With backstepping control designed for different operating conditions, improved convergence for tracking as well as steady-state errors are accomplished. In addition, with local information only, a sophisticated control scheme for decentralized control omits complicated communication networks. Lyapunov theory helps to derive the asymptotic stability of the system, with meticulous observation of currents, powers, as well as disturbances, making the microgrid more reliable.

The rest of this paper proceeds as follows. Section 2 addresses configuration and modeling of the DC microgrid. Section 3 presents the design procedure of the proposed wind and PV sources' controller and observer, with a stability study. Section 4 addresses developing the proposed DC bus voltage regulator controller and observer, with a relevant stability analysis. Section 5 addresses designing a controller and disturbance observer for DC and AC load voltages, with a relevant stability study.

Section 6 shows simulation results that verify the performance of the proposed controller for various operating conditions. Finally, Section 7 concludes the paper with a summary of major findings.

2. DC Microgrid configuration and modeling

2.1. DC Microgrid configuration

The architecture of the DC microgrid system under investigation is illustrated in Figure 1. Two electric sources, a PV generator and a wind source, form the microgrid system. These sources were interfaced to the DC bus by using boost converters. The battery compensates between the energy generation and the load as the storage element of the microgrid. The buck-boost converter enables the connection of the battery to the DC bus. A single-phase full-bridge inverter supplies the AC load and a DC–DC buck converter is used to connect the load to simulate the DC load. The electrical diagram of a DC microgrid is illustrated in Figure 2 [41–43].

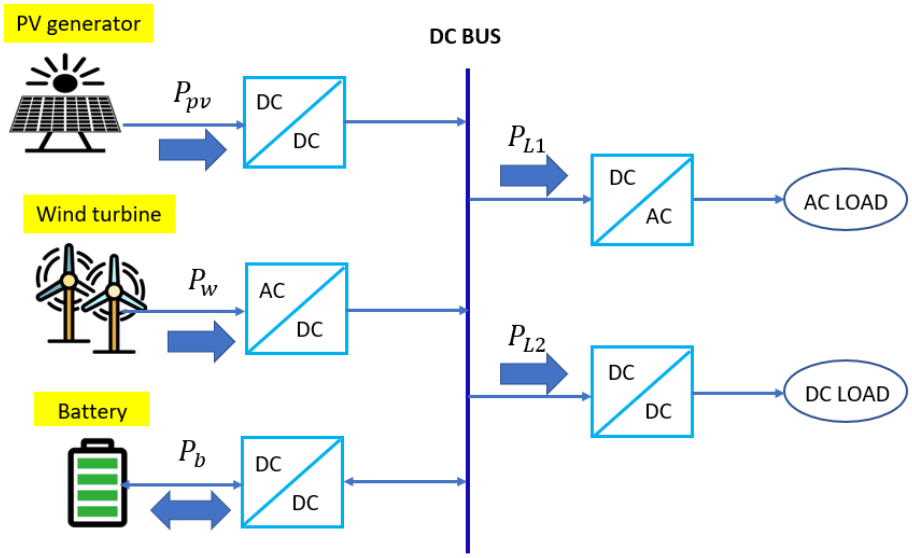

Figure 1. DC microgrid system configuration.

2.2. DC microgrid modeling

The DC microgrid system depicted in Figure 2 was modeled in this section. The converter control signals were built using the control technique suggested in this study and were derived from the microgrid system model. The structure shown in Figure 2 includes the wind turbines, PV sources, and batteries. The PV and wind sources operate in an MPPT configuration. The power delivery capacity of the battery source is calculated based on the DC bus voltage reference provided by the droop control. Climate conditions affect the PV and wind power fed into the shared DC bus of the DC microgrid. Depending on its state of charge (SoC), a battery normally functions in one of two charging modes: constant voltage (CV) or constant current. In the continuous current mode, the charging current remains constant, but the terminal voltage increases.

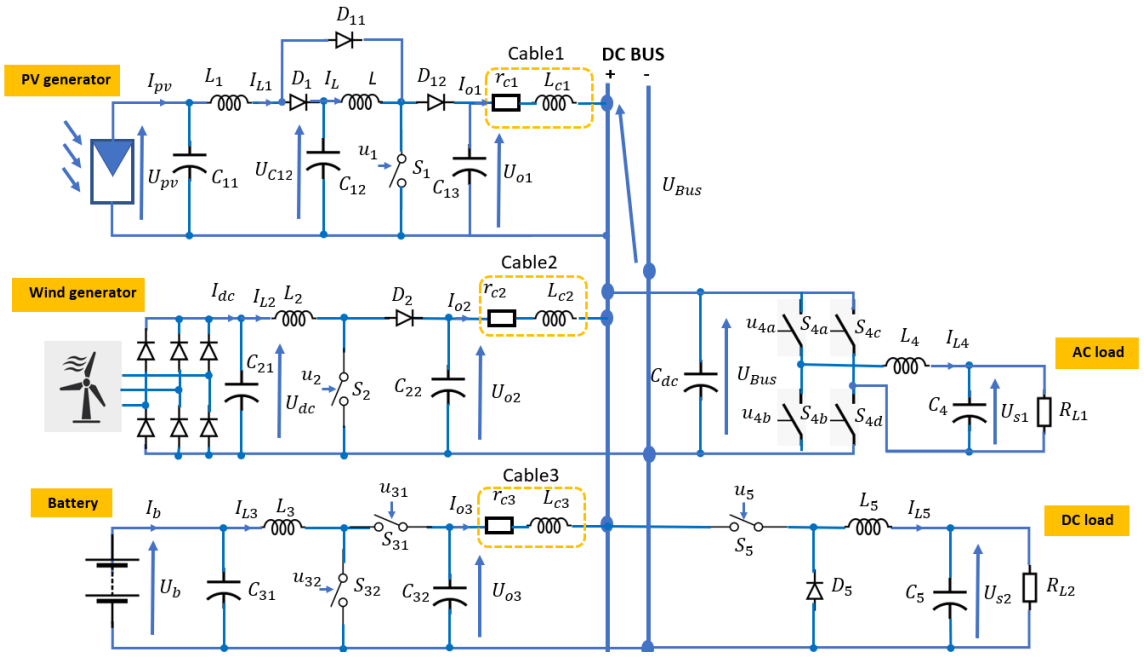

Figure 2. Electrical diagram of the DC microgrid.

2.2.1. Quadratic boost converter model

Because the quadratic boost converter (QBC) has a higher gain than the standard converter, it is more appropriate for the PV source voltage, which is often low, and DC bus voltage, which is relatively high. Figure 2 shows a circuit schematic of the QBC topology. The main component of this setup is an extra boost stage, and an additional active switch is not included. The switching losses in the converter decrease when a single active switch is used. In conclusion, this converter increases the gain of the conventional step-up architecture by combining two boost converters with a single active switch [44]. Eleven parallel strings, each with nine series-connected 213 W modules, were combined to form a PV source with a 21.1 kW capacity. The PV source can inject energy into the common DC bus using the QBC. Depending on the operating mode imposed by the microgrid system energy management algorithm, the PV source operates at the MPP point or to the left (the energy management algorithm is not examined in this study). These are the dynamic equations for QBC [45]:

$$\begin{aligned}
\frac{dU_{pv}}{dt} &= \frac{I_{pv}}{C_{11}} - \frac{I_{L1}}{C_{11}}, \\
\frac{dI_{L1}}{dt} &= \frac{U_{pv}}{L_1} - \frac{(1-\alpha_1).U_{c12}}{L_1}, \\
\frac{dI_L}{dt} &= \frac{U_{c12}}{L} - \frac{(1-\alpha_1).U_{o1}}{L}, \\
\frac{dU_{c12}}{dt} &= -\frac{I_L}{C_{12}} + \frac{(1-\alpha_1).I_{L1}}{C_{12}}, \\
\frac{dU_{o1}}{dt} &= -\frac{I_{o1}}{C_{13}} + \frac{(1-\alpha_1).I_L}{C_{13}},
\end{aligned} \tag{1}$$

where the currents in the PV source, L_1 inductor, and L inductor are I_{pv}, I_{L1}, and I_L, respectively. The voltage across capacitor C_{12} is represented by U_{c12} and the PV voltage by U_{pv}. The QBC output voltage

is denoted by U_{o1} and the output current is denoted by I_{o1}. At the input and output of the QBC, the capacitors are denoted by C_{11} and C_{13}, respectively. Following pulse-width modulation (PWM), the power switch is controlled by duty cycle α_1, whose value ranges from 0 to 1.

2.2.2. Boost converter model

In the considered wind energy system (WES), the wind turbines are connected to the DC bus through a permanent-magnet synchronous generator (PMSG), an unregulated rectifier, and a boost converter. WES configuration is illustrated in Figure 2. The particular option is a PMSG based turbine system, due to its simple controllability, low cost and easy assembling. Utilizing turbines and corresponding PMSG, WESC farming harnesses the wind flows for electrical energy. The mechanical power of a WES can be calculated with the following formula [46–48]:

$$P_w = \frac{1}{2}\rho.\pi.C_p(\lambda,\beta).R^2.V^3, \tag{2}$$

where V is the wind speed, C_p is the power coefficient, R is the turbine radius, and ρ is air density. The pitch angle and relative speed are denoted as β and λ, respectively. In this study, we used a pitch angle of zero (β = 0).

The following equations describe the operation of the boost converter associated with the wind source [43]:

$$\begin{cases} \frac{dU_{dc}}{dt} = \frac{I_{dc}}{C_{21}} - \frac{I_{L2}}{C_{21}}, \\ \frac{dI_{L2}}{dt} = \frac{U_{dc}}{L_2} - \frac{(1-\alpha_2).U_{o2}}{L_2}, \\ \frac{dU_{o2}}{dt} = -\frac{I_{o2}}{C_{22}} + \frac{(1-\alpha_2).I_{L2}}{C_{22}}, \end{cases} \tag{3}$$

where I_{dc} and U_{dc} denote the output voltage and current, respectively, of the three-phase rectifier. The output current and voltage of the boost converter are denoted by I_{o2} and U_{o2}, respectively. L_2 inductor current and duty cycle are represented by I_{L2} and α_2, respectively. The input and output of the boost converter are capacitors, denoted by C_{21} and C_{22}, respectively.

2.2.3. Reversible Buck-boost converter model

An integrated DC microgrid battery energy storage system (BESS) controls the power balance of the system. The energy storage unit charges the system to absorb energy when the output power of the PV and wind production unit is greater than the absorbed power of the loads; on the other hand, the energy storage unit discharges energy to supply the system with energy. Therefore, the interface converter of the energy-storage unit must be bidirectional. Figure 2 shows a schematic diagram of the bidirectional converter. As illustrated in Figure 2, the BESS is set up with the DC bus through a bidirectional buck-boost converter. Owing to the bidirectional current flow capability of this converter, the BESS can be charged in the buck mode or discharged in the boost mode depending on the load current requirement. The available charge of the battery in relation to its peak charging capacity is indicated by the SOC of the BESS. Because it establishes which energy storage unit and how much of

it should be used by the system-level control, monitoring the SOC is essential. The methods outlined in [49,50] were used to compute the SOC values of the implemented BESS system.

$$SOC_b = SOC_0 + \frac{1}{Q_b}\int_0^t \eta_b I_b d\tau\,, \tag{4}$$

where Q_b, η_b are battery capacity and ampere hour efficiency, and I_b, SOC_b, and SOC_0 denote the battery current, the state of charge, and its beginning value, respectively.

The buck-boost converter equations linked to the BESS can be derived using the following expressions [25,43–46]:

$$\begin{cases} \frac{dU_b}{dt} = \frac{I_b}{C_{31}} - \frac{I_{L3}}{C_{31}}, \\ \frac{dI_{L3}}{dt} = \frac{U_b}{L_3} - \frac{\alpha_3 . U_{o3}}{L_3}, \\ \frac{dU_{o3}}{dt} = -\frac{I_{o3}}{C_{32}} + \frac{\alpha_3 . I_{L3}}{C_{32}}, \end{cases} \tag{5}$$

where U_b and I_b represent the battery voltage and current, respectively. I_{o3} and U_{o3} refer to the buck-boost converter's output current and voltage, respectively. At the input and output of the buck-boost converter, the capacitors are denoted by C_{31} and C_{32}, respectively. I_{L3} and α_3 represent the L_3 inductor current and the duty cycle, respectively.

2.2.4. Single phase inverter model

The AC load is linked to the output of the DC-AC inverter. By delivering a regulated voltage of 220 V RMS at 50 Hz, the inverter was a single-phase full-bridge inverter. An electrical schematic of the inverter is displayed in Figure 2. The equations below illustrate the operation of a single-phase inverter [51,52],

$$\begin{cases} \frac{dU_{S1}}{dt} = \frac{I_{L4}}{C_4} - \frac{U_{S1}}{C_4 . R_{L1}}, \\ \frac{dI_{L4}}{dt} = \frac{U_{Bus} . (2.\alpha_4 - 1)}{L_4} - \frac{U_{S1}}{L_4}, \end{cases} \tag{6}$$

where U_{Bus} and U_{s1} refer to the DC common bus voltage and the voltage across the AC load, respectively. The AC load is represented by R_{L1} and the capacitance at the AC load terminal is C_4. L_4 inductance current and duty cycle are represented by I_{L4} and α_4, respectively.

2.2.5. Buck converter model

The output of the buck converter is connected to the DC load. Power flows in only one direction from the common DC bus to the DC load. A buck converter is the most advantageous choice, as it can function within a voltage range of zero to the standard DC bus voltage. A nominal DC voltage of 500V was supplied through buck converter control. The buck converter circuit is illustrated in Figure 2. The equations determining the buck converter operation are as follows [52–55]:

$$\begin{cases} \frac{dU_{S2}}{dt} = \frac{I_{L5}}{C_5} - \frac{U_{S2}}{C_5.R_{L2}}, \\ \frac{di_{L5}}{dt} = \frac{U_{Bus}(\alpha_5 - 1)}{L_5} - \frac{U_{S2}}{L_5}, \end{cases} \tag{7}$$

where U_{s2} denotes the R_{L2} load-terminal voltage. The L_5 inductance current and duty cycle are represented by I_{L5} and α_5, respectively, and the capacitance at the DC load terminal is C_5.

2.2.6. Cables and common DC Bus model

Cables connect various components of the DC microgrid, which are described as inductors and resistors connected in series. The capacitor C_{dc} is a component of the standard DC bus. The following equations represent the DC bus capacitor and link cable models [25–38]:

$$\begin{aligned} \frac{dI_{o1}}{dt} &= \frac{U_{o1}}{L_{c1}} - \frac{U_{Bus}}{L_{c1}} - \frac{r_{c1}.\ I_{o1}}{L_{c1}}, \\ \frac{dI_{o2}}{dt} &= \frac{U_{o2}}{L_{c2}} - \frac{U_{Bus}}{L_{c2}} - \frac{r_{c2}.\ I_{o2}}{L_{c2}}, \\ \frac{dI_{o3}}{dt} &= \frac{U_{o3}}{L_{c3}} - \frac{U_{Bus}}{L_{c3}} - \frac{r_{c3}.\ I_{o3}}{L_{c3}}, \\ \frac{dU_{Bus}}{dt} &= \frac{I_{o1}}{C_{dc}} + \frac{I_{o2}}{C_{dc}} + \frac{I_{o3}}{C_{dc}} - \frac{(2.\alpha_4 - 1).\ I_{L4}}{C_{dc}} - \frac{\alpha_5\ .\ I_{L5}}{C_{dc}}, \end{aligned} \tag{8}$$

where r_{ci} and L_{ci} represent the cable's equivalent resistance and inductance ($i \in \{1, 2, 3\}$), respectively, and the DC bus capacitance is C_{dc}.

3. Backstepping control of PV and wind source

3.1. Integral backstepping control for PV power maximization

All the microgrid system converter switching control signals are determined using the suggested IB control technique [53,54]. Because almost all dynamic models employ the same control methodology, we restricted our scope to the presentation of the final calculation results for the other converters, providing only a step-by-step design process for a QBC converter connected to the PV source.

3.1.1. Extended high-gain observer design of PV current

To minimize the number of sensors, the current I_{pv} is considered an observable disturbance. Estimating disturbance I_{pv} is the primary role of the EHGO. This is due to the fact that utilizing the estimation of I_{pv} will suffice to accomplish the goal of reducing steady state inaccuracy. Thus, it is reasonable to infer that I_{pv} =0. Disturbance I_{pv} is added to the system to construct an EHGO, that is,

$$\begin{cases} \dot{u}_{pv} = \frac{I_{pv}}{C_{11}} - \frac{I_{L1}}{C_{11}}. \\ \dot{I}_{pv} = 0 \end{cases} \tag{9}$$

The augmented system mentioned above can be used to create an EHGO [35],

$$\begin{cases} \dot{\widehat{U}}_{pv} = \frac{\hat{I}_{pv}}{C_{11}} - \frac{\hat{I}_{L1}}{C_{11}} + \frac{2}{\varepsilon_1}\left(U_{pv} - \widehat{U}_{pv}\right) \\ \dot{\hat{I}}_{pv} = \frac{C_{11}}{\varepsilon_1^2}\left(U_{pv} - \widehat{U}_{pv}\right) \end{cases}, \tag{10}$$

where ε_1 is a positive constant that must be chosen as minimal as feasible to obtain a quick estimate. To estimate the PV voltage U_{pv}, use the notation $\widehat{U}_{pv}$.

A PV voltage reference is required by the proposed control design, and the P&O MPPT algorithm generates the requested reference. Figure 3 shows the standard P&O algorithm [56,57].

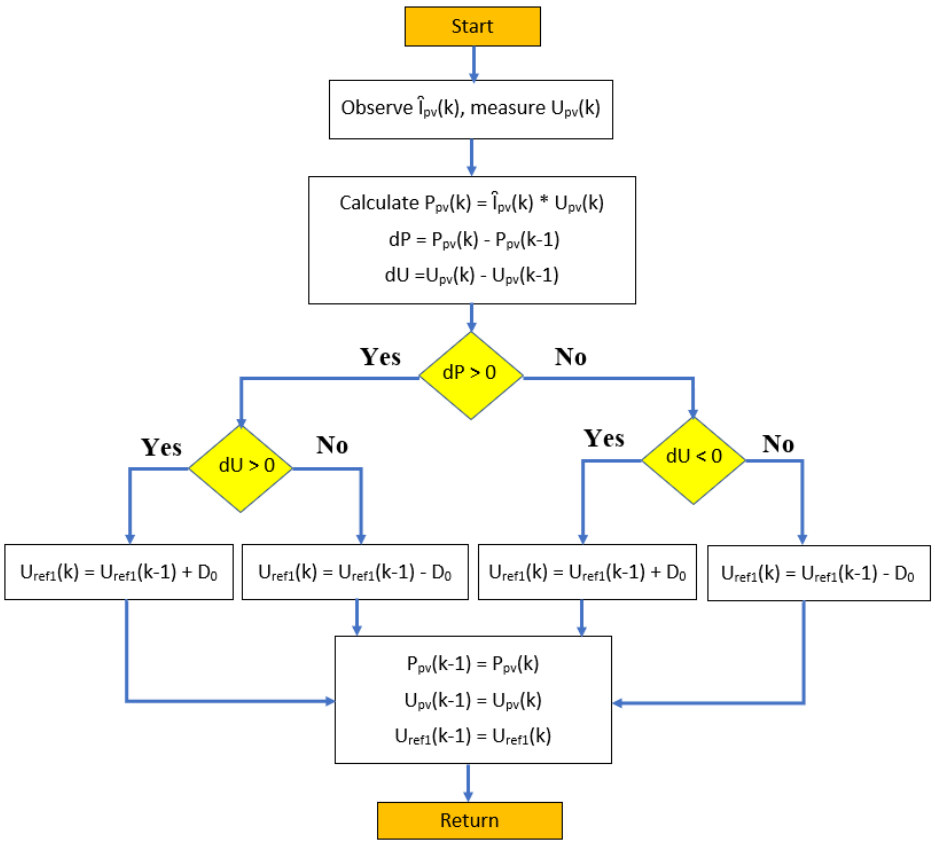

Figure 3. Conventional P&O algorithm for PV generator.

3.1.2. Integral backstepping control of QBC

The proposed control was based on the IB technique [58–60]. The aim is to operate the PV generator at the maximum power.

Step 1. We introduce the following input error, z_{11}:

$$z_{11} = U_{pv} - U_{ref1} + k_{i1}\int U_{pv} - U_{ref1}. \tag{11}$$

The parameter k_{i1} is arbitrary ($k_{i1} \in R$) and U_{ref1} is the reference of PV voltage.

Deriving z_{11} with respect to time and accounting for (1),

$$\dot{z}_{11} = \dot{U}_{pv} - \dot{U}_{ref1} + k_{i1}\left(U_{pv} - U_{ref1}\right) = \frac{I_{pv}}{C_{11}} - \frac{I_{L1}}{C_{11}} - \dot{U}_{ref1} + k_{i1}\left(U_{pv} - U_{ref1}\right), \tag{12}$$

where I_{L1} is the virtual control input. Such an equation shows that one gets $(\dot{z}_{11} = -k_{11}z_{11})$, and $k_{11}>0$ is a design parameter.

Taking into account $\left(\dot{U}_{ref1} = 0\right)$, the stabilizing function is expressed as follows:

$$I_{ref1} = k_{11}C_{11}z_{11} + I_{pv} + k_{i1}.C_{11}.\left(U_{pv} - U_{ref1}\right). \tag{13}$$

The difference between the inductor current and its reference is expressed as:

$$z_{12} = I_{L1} - I_{ref1}. \tag{14}$$

Now, replacing i_{L1} with (z_{12}+I_{ref1}) in (25) yields

$$\dot{z}_{11} = \frac{I_{pv}}{C_{11}} - \frac{\left(z_{12}+I_{ref1}\right)}{C_{11}} + k_{i1}\left(U_{pv} - U_{ref1}\right). \tag{15}$$

By replacing Eq (13) in (15), we obtain

$$\dot{z}_{11} = -k_{11}z_{11} - \frac{z_{12}}{C_{11}}. \tag{16}$$

Step 2. Now, let us examine the behavior of the error variable z_{12}. Equations (1) and (13) were used to obtain the error derivative of z_{12}:

$$\dot{z}_{12} = \dot{I}_{L1} - \dot{I}_{ref1} = \frac{U_{pv}}{L_1} - \frac{U_{c12}}{L_1}(1 - \alpha_1) - \dot{I}_{ref1}. \tag{17}$$

Using expression (13), we calculate the derivative of I_{ref1}

$$\dot{I}_{ref1} = k_{11}C_{11}.\dot{z}_{11} + \dot{I}_{pv} + k_{i1}.C_{11}.\left(\dot{U}_{pv} - \dot{U}_{ref1}\right). \tag{18}$$

Replacing the expressions (1) and (15) in (18), taking into account $\left(\dot{U}_{ref1} = 0\right)$, we obtain:

$$\dot{I}_{ref1} = -k_{11}C_{11}.\left(k_{11}z_{11} + \frac{z_{12}}{C_{11}}\right) + \dot{I}_{pv} + k_{i1}.C_{11}.\left(\frac{I_{pv}}{C_{11}} - \frac{I_{L1}}{C_{11}}\right). \tag{19}$$

By replacing (17) in (19), we obtain the following expression for the error derivative of z_{12}:

$$\dot{z}_{12} = \frac{U_{pv}}{L_1} - \frac{U_{c12}}{L_1}(1 - \alpha_1) + k_{11}C_{11}.\left(k_{11}z_{11} + \frac{z_{12}}{C_{11}}\right) - \dot{I}_{pv} - k_{i1}.\left(I_{pv} - I_{L1}\right). \tag{20}$$

Now we select the Lyapunov function

$$V_1 = 0.5z_{11}^2 + 0.5z_{12}^2. \tag{21}$$

The derivative of the Lyapunov function is calculated by the following expression:

$$\dot{V}_1 = z_{11}\dot{z}_{11} + z_{12}\dot{z}_{12}. \tag{22}$$

Using the expressions (20) and (22), we obtain the expression for the Lyapunov function derivative

$$\dot{V}_1 = -k_{11}z_{11}^2 - k_{12}z_{12}^2 + z_{12}.\left(-\frac{z_{11}}{C_{11}} + k_{12}z_{12} + \dot{z}_{12}\right), \tag{23}$$

where k_{12} is a positive design parameter $(k_{12} > 0)$.

The derivative of the Lyapunov function is negative if the term in the brackets is zero. Hence, the derivative of the error z_{12} must be equal to

$$\dot{z}_{12} = \frac{z_{11}}{C_{11}} - k_{12}z_{12}. \tag{24}$$

By substituting the current I_{pv} with its observation $\hat{I}_{pv}$ and using (20) and (24), the expression of the duty cycle, which allows asymptotic convergence to zero of the errors z_{11} and z_{12}, is

$$\alpha_1 = 1 - \frac{L_1}{U_{c12}}\left(-\frac{z_{11}}{C_{11}} + k_{12}.z_{12} + \frac{U_{pv}}{L_1} + k_{11}C_{11}.\left(k_{11}z_{11} + \frac{z_{12}}{C_{11}}\right) - \dot{\hat{I}}_{pv} - k_{i1}.\left(\hat{I}_{pv} - I_{L1}\right)\right). \tag{25}$$

Figure 4 illustrates the proposed IB control approach for controlling the PV voltage.

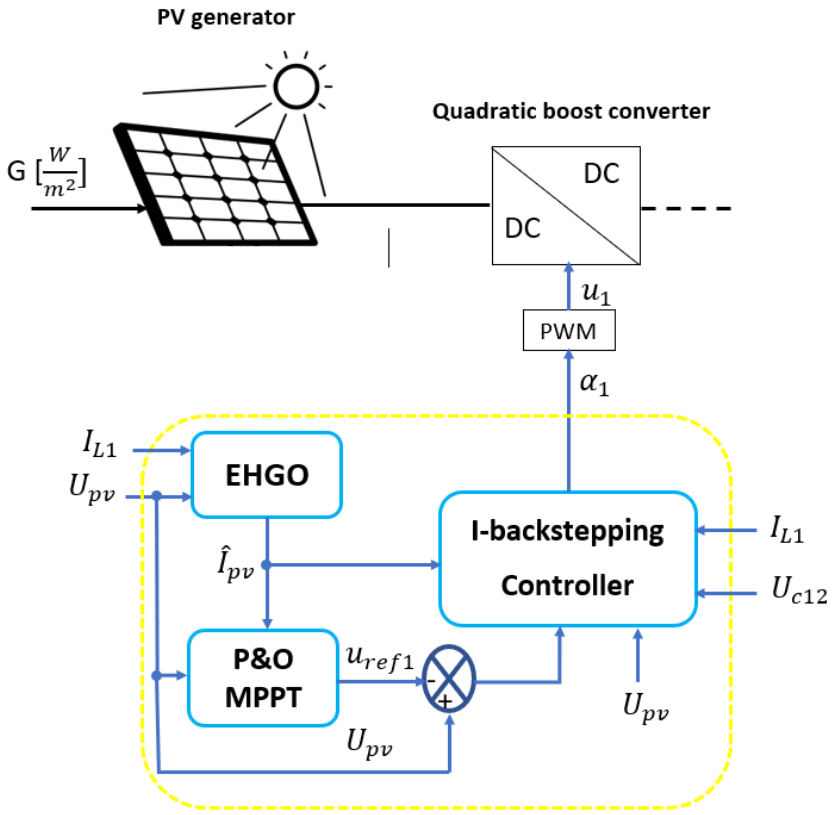

Figure 4. PV Voltage regulation based IB control technique.

3.2. Integral backstepping control for wind power maximization

3.2.1. Extended high-gain observer design of I_{dc} current

Because rectifier losses are not considered, we assume that the power reaching the input of the boost converter is equal to the wind power ($P_w = U_{dc}.I_{dc}$). It seems sensible to conclude that $\left(\dot{I}_{dc} = 0\right)$ based on the study of the high-gain observer for the PV current in the previous section. Disturbance I_{dc} is added to the system to construct an EHGO, that is,

$$\begin{cases} \dot{u}_{dc} = \frac{I_{dc}}{C_{21}} - \frac{I_{L2}}{C_{21}}. \\ \dot{I}_{dc} = 0 \end{cases} \tag{26}$$

The augmented system mentioned above can be used to create an EHGO [35].

$$\begin{cases} \dot{\widehat{U}}_{dc} = \frac{\hat{I}_{dc}}{C_{21}} - \frac{\hat{I}_{L2}}{C_{21}} + \frac{2}{\varepsilon_2}\left(U_{dc} - \widehat{U}_{dc}\right) \\ \dot{\hat{I}}_{dc} = \frac{C_{21}}{\varepsilon_2^2}\left(U_{dc} - \widehat{U}_{dc}\right) \end{cases}, \tag{27}$$

where ε_2 is a positive constant that must be chosen as minimal as feasible to obtain a quick estimate. To estimate the voltage U_{dc}, use the notation $\widehat{U}_{dc}$.

3.2.2. Integral backstepping control of BC

Similar to the previous section, the proposed control was built using the IB technique. In this section, we present an innovative approach based on controlling the voltage at the boost converter input, which delivers the maximum power to operate the wind source, in contrast to earlier research efforts that regulate generator speed. A mechanical speed reference is required to obtain the reference voltage. As shown in Figure 5, the P&O algorithm provides a mechanical speed reference [56,57].

In terms of the output current and electrical speed, the average voltage at the rectifier output is expressed as follows [61]:

$$U_{dc} = \frac{3\sqrt{3}}{\pi}.\psi_m.\Omega_e - \frac{3}{\pi}X_s I_{dc}. \tag{28}$$

The amplitude of the flux linkage in the stator caused by the permanent magnet in the rotor is denoted as ψ_m, where Ω_e and I_{dc} are the electrical speed and rectifier output current, respectively, and X_s is the generator reactance.

Electrical speed is expressed by

$$\Omega_e = P.\Omega_m, \tag{29}$$

where P denotes the number of pole pairs.

The synchronous generator reactance Xs is given by

$$X_s = L_s.P.\Omega_m, \tag{30}$$

where L_s denotes the inductance of the stator phase.

Replacing (29) and (30) in (28) gives the expression for average voltage as a function of mechanical speed

$$U_{dc} = \Omega_m.\left(\frac{3\sqrt{3}}{\pi}.\psi_m.P - \frac{3}{\pi}P.L_sI_{dc}\right). \tag{31}$$

Using (31), we obtain the reference for the average value of the rectifier output voltage

$$U_{ref2} = \Omega_{ref}.\left(\frac{3\sqrt{3}}{\pi}.\psi_m.P - \frac{3}{\pi}.P.L_sI_{dc}\right). \tag{32}$$

The following input error is introduced:

$$z_{21} = U_{dc} - U_{ref2} + k_{i2}\int U_{dc} - U_{ref2}, \tag{33}$$

where the parameter k_{i2} is arbitrary ($k_{i2} \in \Re$).

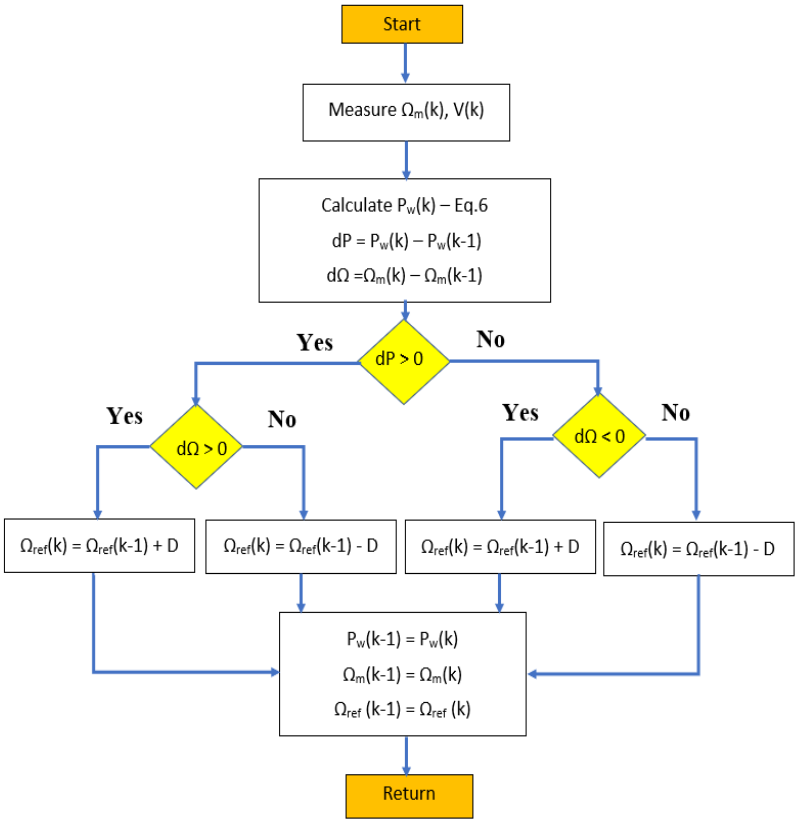

Figure 5. Conventional P&O algorithm for wind generator.

The duty cycle expression for the regulation of the wind generator speed can be obtained by replacing the current I_{dc} with its observed $\hat{I}_{dc}$. This is similar to the design of the PV voltage IB control,

$$\alpha_2 = 1 - \frac{L_2}{U_{o2}}\left(-\frac{z_{21}}{C_{21}} + k_{22}.z_{22} + \frac{U_{dc}}{L_2} + k_{21}C_{21}\left(k_{21}z_{21} + \frac{z_{22}}{C_{21}}\right) - \hat{I}_{dc} - k_{i2}.\left(\hat{I}_{dc} - I_{L2}\right)\right), \tag{34}$$

where k_{21} and k_{22} are design parameters that are positive $(k_{21} > 0, k_{22} > 0)$.

Let us review the expressions for error z_{22} and reference I_{ref2} based on the computation in the previous section,

$$z_{22} = I_{L2} - I_{ref2}.$$

The stabilizing function is expressed as follows:

$$I_{ref2} = k_{21}C_{21}z_{21} + I_{dc} + k_{i2}.C_{21}.\left(U_{dc} - U_{ref2}\right). \tag{36}$$

According to the previous section, the derivative of z_{21} and z_{22} are equal to

$$\dot{z}_{21} = -\frac{z_{22}}{C_{21}} - k_{21}z_{21};\ \dot{z}_{22} = \frac{z_{21}}{C_{21}} - k_{22}z_{22}. \tag{37}$$

Now we select the Lyapunov function

$$V_2 = V_1 + 0.5z_{21}^2 + 0.5z_{22}^2.$$

The derivative of the Lyapunov function is calculated by the following expression

$$\dot{V}_2 = -k_{11}z_{11}^2 - k_{12}z_{12}^2 + z_{21}\dot{z}_{21} + z_{22}\dot{z}_{22}. \tag{38}$$

By replacing (35) and (36) in (38), we obtain the derivative of the Lyapunov function

$$\dot{V}_2 = -k_{11}z_{11}^2 - k_{12}z_{12}^2 - k_{21}z_{21}^2 - k_{22}z_{22}^2. \tag{39}$$

The fact that the Lyapunov function derivative is negative indicates that the system is stable. The IB control concept, corresponding to the maximum power operation of the wind source, is shown in Figure 6.

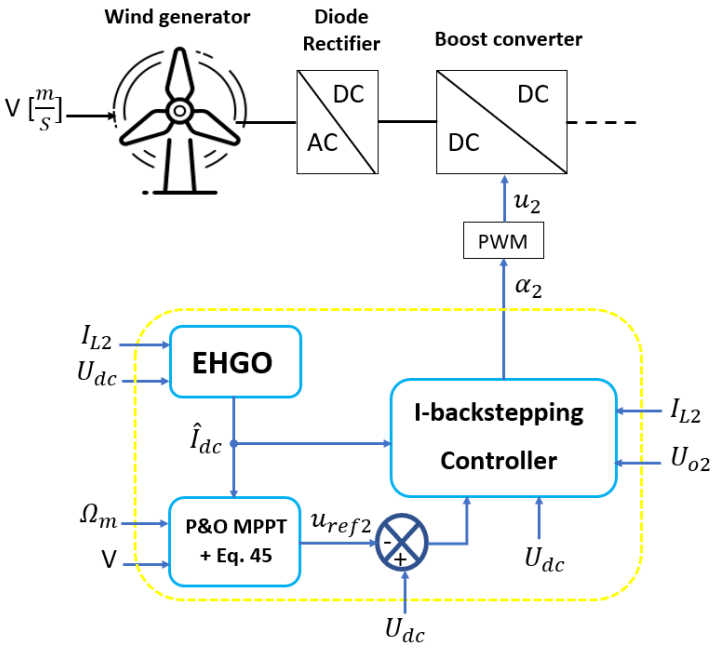

Figure 6. IB control to maximize wind power.

4. Proposed control of the DC bus voltage

In this section, the IB technique for regulating the common DC bus voltage is described. To do this, we installed nonlinear disturbance observers (EHGO, NDO) to measure the load power, as well as the power provided by the PV, wind, and battery.

4.1. Extended high-gain observer design of battery current

The battery current was regarded as an observable disturbance. The principal function of the EHGO is to estimate the disturbance I_b. This is because optimizing for I_b estimation is sufficient to achieve the objective of minimizing the steady-state error. Thus, it is reasonable to infer that $(\dot{I}_b = 0)$ = 0. Disturbance I_b is added to the system to construct an EHGO, that is,

$$\begin{cases} \dot{U}_b = \frac{I_b}{C_{31}} - \frac{I_{L3}}{C_{31}}. \\ \dot{I}_b = 0 \end{cases} \tag{40}$$

The augmented system mentioned above can be used to create an EHGO [35],

$$\begin{cases} \dot{\widehat{U}}_b = \frac{\hat{I}_b}{C_{31}} - \frac{\hat{I}_{L3}}{C_{31}} + \frac{2}{\varepsilon_3}\left(U_b - \widehat{U}_b\right) \\ \dot{\hat{I}}_b = \frac{C_{31}}{\varepsilon_3^2}\left(U_b - \widehat{U}_b\right) \end{cases}, \tag{41}$$

where ε_3 is a positive constant that must be chosen as minimal as feasible to obtain a quick estimate. To estimate the battery voltage U_b, use the notation $\widehat{U}_b$.

4.2. Constructing the nonlinear disturbance observer for estimating PV power

We initially make the following assumptions about the observer design: As disturbance P_1 changes more slowly in the real process than the system state quantity, the time derivative of P_1 can be viewed as zero when compared to the time derivative of the system state. A well-chosen observation gain function can guarantee that a system disturbance is clearly observed [57–62].

For the disturbance observer, the nonlinear system model employed was [63]

$$\dot{x}_1 = f_1(x) + g_{11}(x).u_1 + g_{12}(x).P_1, \tag{42}$$

where $f_1(x)$, $g_{11}(x)$, and $g_{12}(x)$ are smooth curves with respect to the state quantity x_1, u_1 is the system control input, and P_1 is its output.

Refer to Eq (57) using the general model of the system as follows:

$$\begin{pmatrix} \dot{x}_{11} \\ \dot{x}_{12} \end{pmatrix} = \begin{pmatrix} x_{12} \\ U_{c12}\frac{U_{c12}-U_{o1}}{L} + I_L\frac{I_L-I_{o1}}{C_{13}} \end{pmatrix} + \begin{pmatrix} 0 \\ \frac{U_{C12}U_{o1}}{L} - \frac{I_L^2}{C_{13}} \end{pmatrix} u_1 + \begin{pmatrix} -1 \\ 0 \end{pmatrix}.P_1, \tag{43}$$

where $f_1(x) = \begin{pmatrix} x_{12} \\ U_{c12}\frac{U_{c12}-U_{o1}}{L} + I_L\frac{I_L-I_{o1}}{C_{13}} \end{pmatrix}$, $g_{11}(x) = \begin{pmatrix} 0 \\ \frac{U_{C12}U_{o1}}{L} - \frac{I_L^2}{C_{13}} \end{pmatrix}$, $g_{12}(x) = \begin{pmatrix} -1 \\ 0 \end{pmatrix}$, $P_1 = U_{o1}I_{o1}$, $\begin{pmatrix} x_{11} \\ x_{12} \end{pmatrix} = \begin{pmatrix} \frac{1}{2}(L.I_L^2 + C_{13}U_{o1}^2) \\ I_L U_{c12} \end{pmatrix}$, $L_1 = [l_{11} \quad l_{12}]$.

Next, the NDO in Eq (43) is created as follows:

$$\dot{w}_1 = -L_1 g_{12}(x) w_1 - L_1[g_{12}(x).P_a(x) + f_1(x) + g_{11}(x)u_1],$$
$$\hat{P}_1 = w_1 + P_a(x), \tag{44}$$

where L_1 is built as follows, w_1 is the observer's internal state, and $P_a(x)$ is a nonlinear function that has to be designed in the observer.

$$L_1 = \frac{\partial P_a}{\partial x}. \tag{45}$$

The expression for the observed perturbation is obtained by substituting g_{11}, g_{12}, P_a, and L_1,

$$\dot{w}_1 = l_{11}w_1 - l_{11}[I_L U_{c12} - l_{11}x_{11} - l_{12}x_{12}],$$
$$\hat{P}_1 = w_1 + l_{11}x_{11} + l_{12}x_{12}. \tag{46}$$

4.3. Constructing the NDO for estimating wind power

In the following section, P_2, or the power supplied by the wind source in the continuous DC bus, is observed using the same methodology as P_1 in the preceding section [62,63].

For the disturbance observer, the nonlinear system model employed was

$$\dot{x}_2 = f_2(x) + g_{21}(x).u_2 + g_{22}(x).P_2, \tag{47}$$

where $f_2(x)$, $g_{21}(x)$, and $g_{22}(x)$ are smooth curves with respect to the state quantity x_2, u_2 is the system control input, and P_2 is its output.

Refer to Eq (47) using the general model of the system as follows:

$$\begin{pmatrix} \dot{x}_{21} \\ \dot{x}_{22} \end{pmatrix} = \begin{pmatrix} x_{22} \\ \frac{U_{dc}^2}{L_2} + I_{L2}\frac{I_{dc}-I_{L2}}{C_{21}} \end{pmatrix} + \begin{pmatrix} 0 \\ -\frac{U_{o2}.U_{dc}}{L_2} \end{pmatrix} u_2 + \begin{pmatrix} -1 \\ 0 \end{pmatrix}.P_2, \tag{48}$$

where $f_2(x) = \begin{pmatrix} x_{22} \\ \frac{U_{dc}^2}{L_2} + I_{L2}\frac{I_{dc}-I_{L2}}{C_{21}} \end{pmatrix}$, $g_{21}(x) = \begin{pmatrix} 0 \\ -\frac{U_{o2}U_{dc}}{L_2} \end{pmatrix}$, $g_{22}(x) = \begin{pmatrix} -1 \\ 0 \end{pmatrix}$, $P_2 = U_{o2}I_{o2}$, $\begin{pmatrix} x_{21} \\ x_{22} \end{pmatrix} = \begin{pmatrix} \frac{1}{2}(L_2 I_{L2}^2 + C_{22}U_{o2}^2) \\ I_{L2}U_{dc} \end{pmatrix}$, $L_2 = [l_{21} \quad l_{22}]$.

Next, the NDO in Eq (48) is created as follows:

$$\dot{w}_2 = -L_2 g_{22}(x) w_2 - L_2[g_{22}(x).P_b(x) + f_2(x) + g_{21}(x)u_2], \tag{49}$$
$$\hat{P}_2 = w_2 + P_b(x),$$

where L_2 is built as follows: w_2 is the observer's internal state, and $P_b(x)$ is a nonlinear function that must be designed by the observer,

$$L_2 = \frac{\partial P_b}{\partial x}. \tag{50}$$

The expression for the observed perturbation is obtained by substituting g_{21}, g_{22}, P_b, and L_2,

$$\begin{aligned} \dot{w}_2 &= l_{21}w_2 - l_{21}[I_{L2}U_{dc} - l_{21}x_{21} - l_{22}x_{22}], \\ \hat{P}_2 &= w_2 + l_{21}x_{21} + l_{22}x_{22}. \end{aligned} \tag{51}$$

4.4. Constructing the NDO for estimating battery power

The battery power supply/absorption from the DC bus is observed in the following section using the same technique as in the preceding section [62,63].

For the disturbance observer, the nonlinear system model employed was

$$\dot{x}_3 = f_3(x) + g_{31}(x).u_{31} + g_{32}(x).P_3, \tag{52}$$

where $f_3(x)$, $g_{31}(x)$, and $g_{32}(x)$ are smooth curves with respect to the state quantity x_3, u_3 is the system control input, and P_3 is its output.

Refer to Eq (52), using the general model of the system:

$$\begin{pmatrix} \dot{x}_{31} \\ \dot{x}_{32} \end{pmatrix} = \begin{pmatrix} x_{32} \\ \frac{U_b^2}{L_1} + I_{L3}\frac{I_b - I_{L3}}{C_{31}} \end{pmatrix} + \begin{pmatrix} 0 \\ -\frac{U_{o3}U_b}{L_1} \end{pmatrix} u_{31} + \begin{pmatrix} -1 \\ 0 \end{pmatrix}.P_3, \tag{53}$$

where $f_3(x) = \begin{pmatrix} x_{32} \\ \frac{U_b^2}{L_3} + I_{L3}\frac{I_b - I_{L3}}{C_{31}} \end{pmatrix}$, $g_{31}(x) = \begin{pmatrix} 0 \\ -\frac{U_{o3}U_b}{L_3} \end{pmatrix}$, $g_{32}(x) = \begin{pmatrix} -1 \\ 0 \end{pmatrix}$, $P_3 = U_{o3}I_{o3}$, $\begin{pmatrix} x_{31} \\ x_{32} \end{pmatrix} = \begin{pmatrix} \frac{1}{2}(L_3 I_{L3}^2 + C_{32}U_{o3}^2) \\ I_{L3}U_b \end{pmatrix}$, $L_3 = [l_{31} \quad l_{32}]$.

Next, the NDO in Eq (53) is created as follows:

$$\begin{aligned} \dot{w}_3 &= -L_3 g_{32}(x)w_3 - L_3[g_{32}(x).P_c(x) + f_3(x) + g_{31}(x)u_3], \\ \hat{P}_3 &= w_3 + P_c(x), \end{aligned} \tag{54}$$

where L_3 is built as follows: w is the observer's internal state, and $P_c(x)$ is a nonlinear function that must be designed by the observer.

$$L_3 = \frac{\partial P_c}{\partial x}. \tag{55}$$

The expression for the observed perturbation is obtained by substituting g_{31}, g_{32}, P_c, and L_3,

$$\begin{aligned} \dot{w}_3 &= l_{31}w_3 - l_{31}[I_{L3}U_b - l_{31}x_{31} - l_{32}x_{32}], \\ \hat{P}_3 &= w_3 + l_{31}x_{31} + l_{32}x_{32}. \end{aligned} \tag{56}$$

4.5. Constructing the EHGO for estimating load power

Power consumption estimation for both DC and AC loads is required in the duty-cycle formulation of the buck-boost converter. Similarly, to the previous part, which examined the EHGO for the I_{pv}, I_{dc}, and I_b current, it is reasonable to infer that $(\dot{P}_L = 0)$. Based on (8), the disturbance P_L is added to the system to construct an EHGO, that is,

$$\begin{cases} \dot{x} = \frac{2}{C_{dc}}(U_{Bus}.I_{o1} + U_{Bus}.I_{o2} + U_{Bus}.I_{o3}) - \frac{2}{C_{dc}}P_L \\ \dot{P}_L = 0 \end{cases}, \tag{57}$$

where the DC bus voltage square is denoted by the variable x. $(x = U_{Bus}^2)$.

By ignoring switching losses in power switches and Joule losses in the three connection cables, the powers provided by the PV generator, the wind source, and the BESS in the common DC bus are denoted as $(U_{Bus}I_{o1})$, $(U_{Bus}I_{o2})$, and $(U_{Bus}I_{o3})$, accordingly. We obtain

$$\begin{cases} P_1 = P_{pv} = U_{Bus}I_{o1} \\ P_2 = P_w = U_{Bus}I_{o2} \\ P_3 = P_b = U_{Bus}I_{o3} \end{cases}. \tag{58}$$

The augmented system mentioned above can be used to create an EHGO [35],

$$\begin{cases} \dot{\hat{x}} = \frac{2}{C_{dc}}(\hat{P}_1 + \hat{P}_2 + \hat{P}_3) - \frac{2}{C_{dc}}\hat{P}_L + \frac{2}{\varepsilon_4}(x - \hat{x}) \\ \dot{\hat{P}}_L = \frac{C_{dc}}{\varepsilon_4^2}(x - \hat{x}) \end{cases}, \tag{59}$$

where ε_4 is a positive constant that must be chosen as minimal as feasible to obtain a quick estimate. To estimate x, use the notation $\hat{x}$.

4.6. IB common DC bus voltage droop control

A crucial element in ensuring that a microgrid runs properly is to control the common DC bus voltage. It is possible to balance the production and consumption of electrical energy by controlling battery power. To control the DC bus voltage, a buck-boost converter is designed using IB control, as explained in this section. Using battery current control (CC mode), the event that the battery is not charged is one of two probable possibilities. In the second scenario, the battery is charged, but it must be allowed to reach its maximum voltage or explode. In this case, the battery voltage must be controlled to its nominal value (CV mode) [41,64].

Based on (57) and (58), we obtain the following expression:

$$\dot{x} = \frac{2}{C_{dc}}(P_{pv} + P_w + P_b - P_L) = \frac{2}{C_{dc}}P_b + f_1(P_{pv}, P_w, P_L). \tag{60}$$

Considering the simplistic assumptions mentioned above and neglecting the change in battery current $(\dot{I}_b \cong 0)$, the battery power derivative is expressed by

$$\dot{P}_b = -\frac{U_b U_{o3}}{L_3}.\alpha_3 + f_2(I_b, I_{L3}, U_b), \tag{61}$$

where $f_1(P_{pv}, P_w, P_L) = \frac{2}{C_{dc}}(P_{pv} + P_w - P_L)$ and $f_2(I_b, I_{L3}, U_b) = \frac{I_b^2}{C_{31}} - \frac{I_b.I_{L3}}{C_{31}} + \frac{U_b^2}{L_3}$.

By employing Eq (58), the DC bus voltage reference is obtained from the droop control output [42,48,57,62]:

$$U_{Bus-ref} = U_{ref} - m.\hat{P}_3, \tag{62}$$

where m denotes the droop control coefficient, and U_{ref} is the voltage reference value prior to droop control.

The following input error is introduced:

$$z_{31} = x - x_{ref} + k_{i3}\int x - x_{ref}, \tag{63}$$

where $x_{ref} = u_{Bus-ref}^2$ and the parameter k_{i3} is arbitrary ($k_{i2} \in \Re$).

By employing Eq (58), the powers P_{pv}, P_w, P_b, and P_L are replaced with $\hat{P}_1$, $\hat{P}_2$, $\hat{P}_3$ and $\hat{P}_L$ respectively. Current I_b was replaced with the observed value $\hat{I}_b$. We derive the duty cycle equation for DC bus regulation, as in earlier sections.

$$\alpha_3 = \frac{L_3}{U_b.U_{o3}}\begin{pmatrix} \frac{z_{31}}{C_{31}} + k_{32}.z_{32} + \frac{\hat{I}_b^2}{C_{31}} - \frac{\hat{I}_b I_{L3}}{C_{31}} + \frac{U_b^2}{L_3} + k_{31}\frac{C_{dc}}{2}\left(-k_{31}z_{31} + \frac{z_{32}}{C_{31}}\right) \\ +k_{i3}.(\hat{P}_1 + \hat{P}_2 + \hat{P}_3 - \hat{P}_L) + \left(\dot{\hat{P}}_1 + \dot{\hat{P}}_2 - \dot{\hat{P}}_L\right) \end{pmatrix}, \tag{64}$$

where k_{31} and k_{32} are design parameters that are positive $(k_{31} > 0, k_{32} > 0)$.

Let us review the expressions for error z_{32} and reference P_{ref} based on the computation in the previous section.

$$z_{32} = P_b - P_{ref}. \tag{65}$$

The stabilizing function is expressed as follows:

$$P_{ref} = -\left(k_{31}z_{31} + \frac{2}{C_{dc}}(P_{pv} + P_w - P_L) + k_{i3}.(x - x_{ref})\right)\frac{C_{dc}}{2}. \tag{66}$$

According to the previous section, the derivative of z_{31} and z_{32} are equal to

$$\dot{z}_{31} = \frac{2.z_{32}}{C_{dc}} - k_{31}z_{31},\ \dot{z}_{32} = \frac{2.z_{31}}{C_{dc}} - k_{32}z_{32}. \tag{67}$$

Now, we select the Lyapunov function

$$V_3 = V_2 + 0.5z_{31}^2 + 0.5z_{32}^2. \tag{68}$$

The derivative of the Lyapunov function is calculated by the following expression

$$\dot{V}_3 = -k_{11}z_{11}^2 - k_{12}z_{12}^2 - k_{21}z_{21}^2 - k_{22}z_{22}^2 + z_{31}\dot{z}_{31} + z_{32}\dot{z}_{32}. \tag{69}$$

By replacing (67) in (69), we obtain the derivative of the Lyapunov function

$$\dot{V}_3 = -k_{11}z_{11}^2 - k_{12}z_{12}^2 - k_{21}z_{21}^2 - k_{22}z_{22}^2 - k_{31}z_{31}^2 - k_{32}z_{32}^2. \tag{70}$$

The derivative of the Lyapunov function is negative, which proves that the system is stable.

Figure 7 depicts the concept of common DC bus voltage regulation, battery current observation, and power observations required to create the proposed control law.

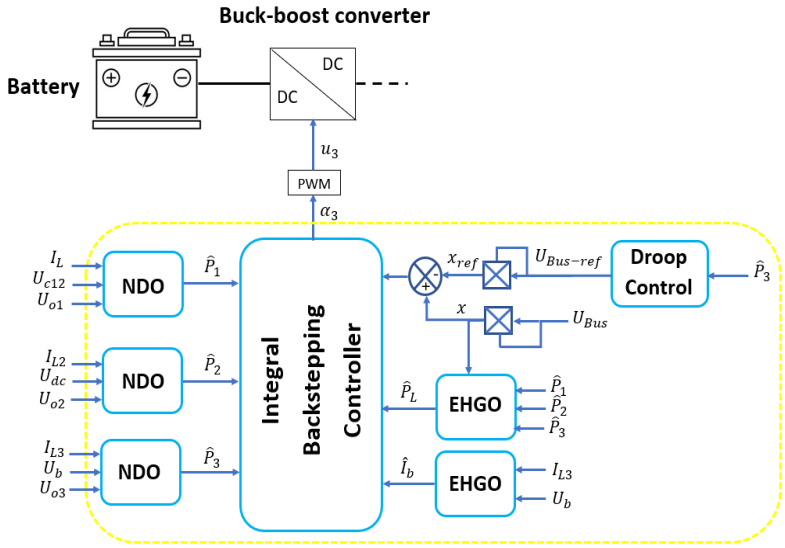

Figure 7. Proposed common DC bus voltage regulation.

5. Design of a backstepping control system for voltage regulation of DC and AC loads

5.1. IB control design of single-phase inverter

The terminal voltage needs must be controlled according to U_{s1ref}, that is, the reference voltage. The IB control, which is covered in detail in the preceding sections, provides the basis for AC voltage regulation.

The following input error is introduced:

$$z_{41} = U_{s1} - U_{s1ref} + k_{i4}\int U_{s1} - U_{s1ref}, \tag{71}$$

where the AC output voltage reference is $U_{s1ref} = U_M \sin(\omega.t)$ and the parameter k_{i4} is arbitrary ($k_{i4} \in \Re$). $(U_M = 311V, \omega = 2.\pi.f, f = 50Hz)$.

The duty cycle equation for AC voltage regulation was obtained in the same manner as in the previous sections.

$$\alpha_4 = \frac{1}{2} + \frac{L_4}{2.U_{Bus}}\begin{pmatrix} -\frac{z_{41}}{C_4} + k_{42}.z_{42} + \frac{U_{s1}}{L_5} + k_{41}C_4\left(k_{41}z_{41} - \frac{z_{42}}{C_4}\right) + C_4\ddot{U}_{s1ref} + \frac{\dot{U}_{s1}}{R_{L1}} \\ -C_4.k_{i2}.\left(\frac{I_{L4}}{C_4} - \frac{U_{s1}}{R_{L1}C_4} - \dot{U}_{s1ref}\right) \end{pmatrix}, \tag{72}$$

where R_{L1} is AC load resistor, k_{41} and k_{42} are design parameters that are positive $(k_{41} > 0, k_{42} > 0)$.

Let us review the expressions for error z_{42} and reference I_{L4ref} based on the computation in the previous section.

$$z_{42} = I_{L4} - I_{L4ref}. \tag{73}$$

The stabilizing function is expressed as follows:

$$I_{L4ref} = -k_{41}C_4 z_{41} + \frac{U_{s1}}{R_{L1}} + C_4.\dot{U}_{s1ref} - k_{i4}.C_4.\left(U_{s1} - U_{s1ref}\right). \tag{74}$$

According to the previous section, the derivative of z_{41} and z_{42} are equal to

$$\dot{z}_{41} = \frac{z_{42}}{C_4} - k_{41}z_{41};\ \dot{z}_{42} = -\frac{z_{41}}{C_4} - k_{42}z_{42}. \tag{75}$$

Now we select the Lyapunov function

$$V_4 = V_3 + 0.5z_{41}^2 + 0.5z_{42}^2. \tag{76}$$

The derivative of the Lyapunov function is calculated by the following expression

$$\dot{V}_4 = -k_{11}z_{11}^2 - k_{12}z_{12}^2 - k_{21}z_{21}^2 - k_{22}z_{22}^2 - k_{31}z_{31}^2 - k_{32}z_{32}^2 + z_{41}\dot{z}_{41} + z_{42}\dot{z}_{42}. \tag{77}$$

By replacing (75) in (77), we obtain the derivative of the Lyapunov function

$$\dot{V}_4 = -k_{11}z_{11}^2 - k_{12}z_{12}^2 - k_{21}z_{21}^2 - k_{22}z_{22}^2 - k_{31}z_{31}^2 - k_{32}z_{32}^2 - k_{41}z_{41}^2 - k_{42}z_{42}^2. \tag{78}$$

The derivative of the Lyapunov function is negative, which proves that the system is stable.

The principle of controlling the AC load terminal voltage using the IB technique is illustrated in Figure 8.

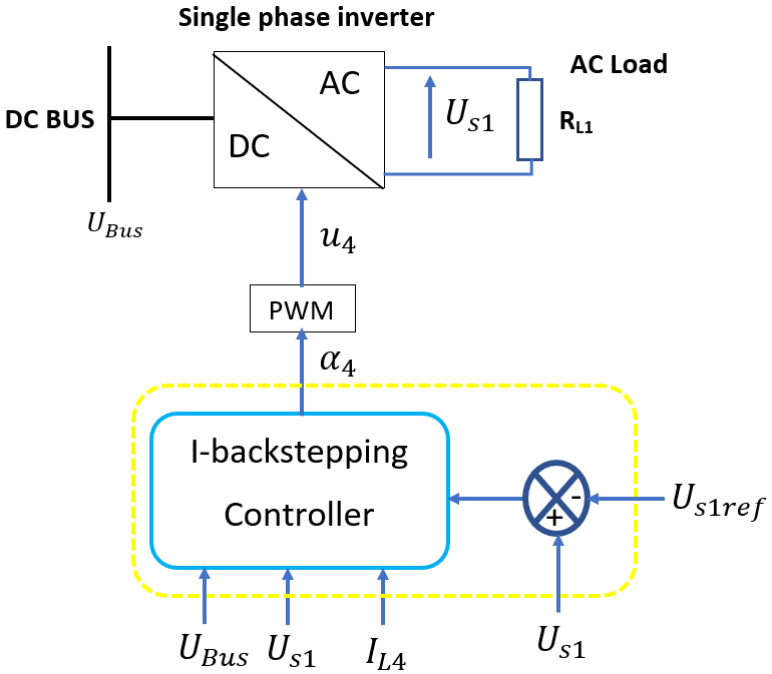

Figure 8. IB regulation of the AC load voltage.

5.2. IB control and DC load perturbation observer design

It is necessary to regulate the DC load terminal voltage to its reference value. Depending on a variety of external factors, including temperature, the DC load resistance R_{L2} in the circuit may fluctuate continuously [62]. Assumed to be R_0 is the nominal value of R_{L2}. The dynamic model of the buck converter is inferred based on Eqs (7) and (8),

$$\frac{dx_{1a}}{dt} = x_{2a} + d_1(t),$$

$$\frac{dx_{2a}}{dt} = u - \frac{x_{1a}}{L_5C_5} - \frac{x_{2a}}{R_0C_5} + d_2(t), \tag{79}$$

where $x_{1a} = U_{s2} - U_{s2ref}$ and $x_{2a} = \frac{I_{L5}}{C_5} - \frac{U_{s2}}{C_5.R_0}$ $d_1(t) = \frac{U_{s2}}{R_0C_5} - \frac{U_{s2}}{R_{L2}C_5}$, $d_2(t) = -\frac{1}{R_0C_5}\left[\frac{U_{s2}}{R_0C_5} - \frac{U_{s2}}{R_{L2}C_5}\right]$, $u = \frac{\alpha_5.U_{Bus} - U_{s2ref}}{L_5C_5}$, R_{L2} is the DC load resistor, $d_1(t)$ and $d_2(t)$ are disturbances produced by uncertainty in the R_{L2} load, and U_{s2ref} is the reference voltage U_{s2}.

5.2.1. Extended observer state (ESO) design for perturbation estimation

This section describes the development of a disturbance estimator to identify the disturbances produced by changes in the DC load resistor. Using the mathematical model of the buck converter, the ESO technique was used to estimate mismatched disturbances in $d_1(t)$ [57,65],

$$\dot{\hat{x}}_{1a} = \hat{x}_{2a} + \hat{d}_1 - \gamma_1(\hat{x}_{1a} - x_{1a}), \tag{80}$$

$$\dot{\hat{d}}_1 = -\gamma_2(\hat{x}_{1a} - x_{1a}),$$

where $\hat{x}_{1a}$ and $\hat{x}_{2a}$ are the estimates of x_{1a} and x_{2a}, respectively, $\hat{d}_1$ and $\hat{d}_2$ are the estimate of d_1 and d_2, respectively, γ_1 and γ_2 are positive parameters $(\gamma_1 > 0,\ \gamma_2 > 0)$.

The matched disturbance estimate of $d_2(t)$ is immediately calculated from the $\hat{d}_1$, provided by

$$\hat{d}_2 = -\frac{\hat{d}_1}{R_0C_5}. \tag{81}$$

5.2.2. IB regulation of the DC load voltage

The output voltage regulation is based on IB control, which has been discussed in detail in previous sections.

The following input error is introduced:

$$z_{51} = x_{1a} + k_{i5}\int x_{1a}. \tag{82}$$

The parameter k_{i5} is arbitrary ($k_{i5} \in \Re$).

Similar to the earlier parts, we obtain the following expression for the duty cycle for DC load voltage regulation:

$$\alpha_5 = \frac{U_{s2ref}}{U_{Bus}} + \frac{L_5 C_5}{U_{Bus}} \begin{pmatrix} -z_{51} - k_{52}.z_{52} + \frac{x_{1a}}{L_5 C_5} + \frac{x_{2a}}{R_0 C_5} - \hat{d}_2 - k_{51}(-k_{51} z_{51} + z_{52}) \\ . \\ -\hat{d}_1 - k_{i5}(x_{2a} + \hat{d}_1) \end{pmatrix}, \tag{83}$$

where k_{51} and k_{52} are design parameters that are positive $(k_{51} > 0, k_{52} > 0)$.

Let us review the expressions for error z_{52} and reference x_{2ref} based on the computation in the previous section,

$$z_{52} = x_{2a} - x_{2ref}. \tag{84}$$

The stabilizing function is expressed as follows:

$$x_{2ref} = -k_{51} z_{51} - \hat{d}_1 - k_{i5}.x_{1a}. \tag{85}$$

According to the previous section, the derivative of z_{51} and z_{52} is equal to

$$\dot{z}_{51} = z_{52} - k_{51} z_{51}, \tag{86}$$

$$\dot{z}_{52} = -z_{51} - k_{52} z_{52}.$$

Now we select the Lyapunov function

$$V_5 = V_4 + 0.5 z_{51}^2 + 0.5 z_{52}^2. \tag{87}$$

The derivative of the Lyapunov function is calculated by the following expression

$$\begin{aligned} \dot{V}_5 = &-k_{11} z_{11}^2 - k_{12} z_{12}^2 - k_{21} z_{21}^2 - k_{22} z_{22}^2 - k_{31} z_{31}^2 \\ &-k_{32} z_{32}^2 - k_{41} z_{41}^2 - k_{42} z_{42}^2 + z_{51} \dot{z}_{51} + z_{52} \dot{z}_{52}. \end{aligned} \tag{88}$$

By replacing (86) in (88), we obtain the derivative of the Lyapunov function

$$\begin{aligned} \dot{V}_5 = &-k_{11} z_{11}^2 - k_{12} z_{12}^2 - k_{21} z_{21}^2 - k_{22} z_{22}^2 - k_{31} z_{31}^2 \\ &-k_{32} z_{32}^2 - k_{41} z_{41}^2 - k_{42} z_{42}^2 - k_{51} z_{51}^2 - k_{52} z_{52}^2. \end{aligned} \tag{89}$$

The derivative of the Lyapunov function is negative, which proves that the system is stable.

Figure 9 depicts the process of observing d_1 and d_2 disturbances using the ESO and controlling the DC load voltage by employing the proposed control technique.

To ensure voltage and frequency stability in the proposed hybrid renewable-based DC microgrid, the IB controller is designed to regulate the common DC bus voltage while coordinating the operation of PV, wind, and battery subsystems. The inclusion of integral action eliminates steady-state errors, thereby guaranteeing tight voltage regulation under both generation and load variations. In grid-connected operation, frequency stability is preserved by ensuring that the inverter output remains synchronized with the grid through appropriate control of the DC-AC conversion stage. The nonlinear observers further enhance robustness by providing accurate state and disturbance estimation, which allows the controller to compensate for fluctuations in renewable generation and load demand. By combining these mechanisms, the proposed framework ensures stable voltage and frequency dynamics across a wide range of hybrid system operating scenarios.

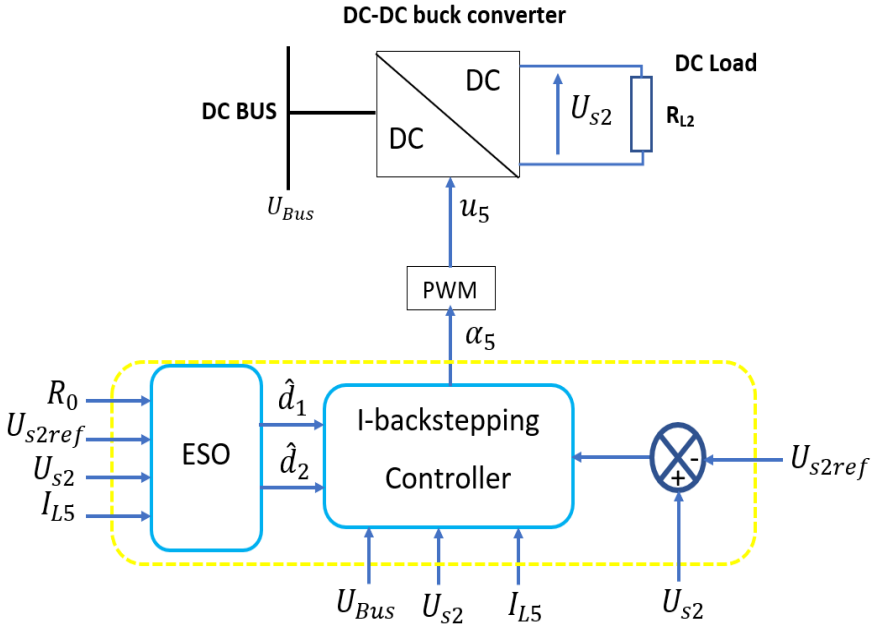

Figure 9. IB regulation of DC load voltage ethics approval of research.

6. Simulation results

The simulation results were used to validate the suggested IB. The configuration of the test system, that is, a DC microgrid, was considered for this purpose. Using DC-DC converters, the PV, wind, and battery sources in the test system depicted in Figure 2 were connected to the DC bus as a DC microgrid. Load charge converters are closed-loop DC-DC buck devices that function as CPLs. Under typical climatic conditions, the solar PV unit can provide up to 21 kW of power with a desired DC bus voltage of 1000 V. It was assumed that the PMSG-based wind farm would have a rated production capacity of 21 kW. A 200 Ah capacity lithium-ion battery with a nominal voltage of 500 V was used for the BESS. The nominal load requirement of an AC bus is 4.84 kW, whereas that of a DC bus is 25 kW. The converter switching frequency in the simulation was fixed at 5 kHz. Table 1 summarizes these system parameters. Table 2 provides the parameters for both the observers and the IB controllers.

To improve reproducibility, the hardware and software environment used in this study is explicitly described. All simulations were conducted in MATLAB/Simulink R2023a on a workstation equipped with an Intel Core i7 processor (3.6 GHz) and 32 GB RAM, providing sufficient computational capacity for high-fidelity switching and nonlinear dynamic modeling. The ode45 solver with variable step size was used, with a relative tolerance of 1×10^{-6} and an average control sampling time of 1×10^{-4} s, corresponding to the converter switching frequency of 5 kHz. The PV, wind, and battery subsystems were integrated with their respective DC–DC converters and load converters using standard Simulink power electronics blocks. Controller and observer parameters (Table 2) were implemented through embedded MATLAB functions, and modularity was ensured via subsystem-based signal routing. Initial conditions—such as PV open-circuit voltage, wind turbine angular speed, and battery state of charge—were defined according to typical operating values, while time-varying disturbance profiles (irradiance and wind speed variations) were applied externally to test robustness.

Table 1. Test system specifications.

Parameter	Value	Parameter	Value
PV generator		Cables	
Max PV power (P_{Pv_max})	21 kW	Resistor ($r_{C1} = r_{C2} = r_{C3}$)	0.1 Ω
Max PV voltage (U_{Pv_max})	261 V	Inductor ($L_{C1} = L_{C2} = L_{C3}$)	10 mH
Max PV current (I_{Pv_max})	80.85 A	DC Bus	
Open-circuit voltage (V_{oc})	326.7 V	DC bus voltage (U_{ref})	1000 V
Short circuit current (I_{sc})	86.24 A	DC Bus Capacitor (C_{dc})	5000 µF
Wind turbine		Buck converter	
Power coefficient (C_p)	0.43	Inductors (L_5)	10 mH
Max wind power (P_{w_max})	20 kW	Capacitor (C_5)	1000 µF
Blade radius (R)	4 m	Load Resistance (R_{L2})	10 Ω
Battery		Nominal output voltage (U_{s2})	500 V
Battery nominal voltage (U_B)	500 V	Single phase inverter	
Battery rated capacity (C_B)	200 Ah	Inductors (L_4)	3 mH
Quadratic boost converter		RMS output voltage (U_{s1_RMS})	220 V
Inductors (L_1)	10 mH	Capacitor (C_4)	500 µF
Inductors (L)	10 mH	Load Resistance (R_{L1})	10 Ω
Capacitor (C_{11})	500µF	Buck-boost converter	
Capacitor (C_{12})	500µF	Inductors (L_3)	10 mH
Capacitor (C_{13})	20µF	Capacitor (C_{31})	100 µF
Boost converter		Capacitor (C_{32})	20 µF
Inductors (L_2)	10 mH		
Capacitor (C_{21})	1000µF		
Capacitor (C_{22})	20µF		

Table 2. IB controller, observer, and MPPT parameters.

	k_{11}	k_{12}	k_{i1}		EHGO	
	1	100	100		ε_1	10^{-5}
	k_{21}	k_{22}	k_{i2}		ε_2	10^{-5}
	1	100	1000		ε_3	10^{-4}
Integral	k_{31}	k_{32}	k_{i3}		ε_4	10^{-4}
Backstepping	1	200	100	Observers	**NDO**	
controller	k_{41}	k_{42}	k_{i4}		l_{11}, l_{12}	-1000, 0
	1	100	1000		l_{21}, l_{22}	-1000, 0
	k_{51}	k_{52}	k_{i5}		l_{31}, l_{32}	-1000, 0
	1	100	100		**ESO**	
					$\gamma_1 = 500$	$\gamma_2 = 1500$
MPPT (step)	PV	D_0	10^{-4}	Wind	D	5.10^{-4}

To ensure transparency in parameter selection, the following considerations were applied:

- Renewable source ratings: PV and wind generators (21 kW each) were selected to represent a balanced medium-scale hybrid microgrid, consistent with benchmark studies in DC microgrids.
- Battery capacity: A 200 Ah lithium-ion battery (500 V) was used to handle peak load variations and ensure reliable energy buffering without excessive depth of discharge.
- DC bus nominal voltage and switching frequency: The 1000 V bus voltage and 5 kHz switching frequency were chosen in accordance with institute of electrical and electronics engineers (IEEE)-recommended practices for medium-voltage DC systems.
- Controller gains: Gains for the IB strategy were first derived based on Lyapunov stability conditions to guarantee convergence. These values were then refined using a hit-and-trial tuning procedure in simulation, ensuring minimal overshoot, fast settling, and stable operation across all operating conditions.
- Sensitivity analysis: A ±10% variation in inductances, capacitances, and load levels was applied to confirm robustness. The controller consistently maintained voltage regulation and disturbance rejection under these variations.

This methodology ensures that parameter selection is transparent, practically motivated, and robust to uncertainties in system components.

It is important to note that the proposed controller was tested under varying load resistance and external disturbances to reflect real-world uncertainties. The inclusion of disturbance terms $d_1(t)$ and $d_2(t)$ in the model ensures that the controller performance accounts for parameter fluctuations, while the ESO successfully mitigates their effects. Simulation results confirm that voltage stability is preserved despite these uncertainties.

The simulation process begins with the PV generating unit, which stabilizes the DC bus voltage of the proposed microgrid. Subsequently, the BESS, DC load, AC load, and wind generator are sequentially activated. The proposed framework supports a variety of operating scenarios; however, for clarity, two representative cases are selected to demonstrate the effectiveness of the designed IB controller in comparison with the conventional backstepping method [66] for DC bus voltage regulation while supplying power to the loads:

- Case 1: Controller performance under varying generation conditions.
- Case 2: Controller performance under varying load requirements.

Case 1: The controller's performance when the generated power varies.

To evaluate the effectiveness of the proposed controller, this case study considered the fluctuating irradiance in the solar PV unit (Figure 10(a)) and varying wind speeds (Figure 10(b)) of the PMSG. Additionally, it was assumed that the AC demand (4.884 kW) and DC load (25 kW) remained constant. The responses from the two regulators are nearly the same, and Figure 10(c–e) show that the PV voltage, mechanical generator speed, and output rectifier voltage follow the references provided by the MPPT algorithm. The DC load terminal voltage was set to 500V (Figure 10(i)), while the AC load terminal voltage (Figure 10(g)) was set to an RMS value of 220V. However, as shown in fig.10(f), the response of the common bus voltage differed between the proposed and standard commands. During the simulation, the DC bus voltage created by the traditional control is more inaccurate than the voltage provided by the recommended control; however, this inaccuracy reduces after 1.5 seconds. A comparison of the accuracy of the suggested and traditional controls is presented in Table 3. This table unequivocally demonstrates that the DC bus voltage accuracy of the proposed control is higher than that of the conventional control. As previously mentioned, all the control methods reviewed result in nearly equal voltage responses at the terminals of the AC and DC loads, with the exception of the static error,

which in the case of traditional backstepping control is 2.2V in the U_{s2} voltage response (Figure 10(i)). Furthermore, because the irradiance value of the PV unit is set at 1000 W/m^2 and the PV output power is 21 kW, it is assumed that it operates initially under normal weather conditions. This process continues until t = 0.5 s. However, the wind speed was 12 ms^{-1} before t = 1.5 s, and the PMSG-based wind farm generated 21 kW of power at this wind speed. Consequently, the DC bus's overall output power over the 0–0.5 s timeframe is 42 kW, whereas the entire load demand is 29.84 kW, showing that extra power is available. The battery can store additional power. As long as the power does not exceed the battery's maximum charging limit, the remaining 12.16 kW will be stored by the battery. As shown in (Figure 10(j)), this is apparent in the power profiles of the different components until t = 0.5 s. Irradiation falls from 1000 to 800 W/m^2 between 0.5 and 1s, solar power declines to 17 kW, wind power remains at 21 kW, and the total power generated is 38 kW compared to the total demand of 29.84 kW. The battery stores the 8.16 kW of excess power. The irradiance drops from 800 to 600 kW in 1 to 1.5 s, PV power increases from 17 to 12.8 kW, wind power stays constant at 21 kW, total power output is 33.8 kW, and total demand stays constant at 29.84 kW. The battery stores the 3.96 kW of excess power. Between 1.5 and 2 s, the irradiance stays constant at 600 W/m^2, the solar power stays at 12.8 kW, the wind speed drops from 12 to 10 m/s, the wind power drops from 21 kW to 12.2 kW, the total power produced is 25.3 kW, and the total load power is 29.84 kW. The battery supplies a 4.84 kW of the power deficit. Between 2 and 2.5 s, the irradiance is constant at 600 W/m^2, solar power is 12.8 kW, wind speed falls from 10 to 8 m/s, wind power decreases from 12.2 kW to 6 kW, total power output is 18.2 kW, and total power demand from DC and AC loads is 29.84 kW. The battery supplies an 11.64 kW power deficit to maintain power balancing. The actual and observed powers and currents are shown in Figure 10(k) and 10(l), respectively. It is important to note that the observers exhibited superior performance. The power and current observation errors were minimal throughout the simulations.

Table 3. DC bus voltage accuracy $\left|{}^{\Delta U}/_{U}\right| = 100.\left|\frac{U_{Bus}-U_{Bus-ref}}{U_{Bus-ref}}\right|$ for irradiation & speed change.

Time (s)	P_b (kW)	$U_{Bus-ref}$ (V)	Conventional control [66]	Proposed controller
			$\left\|\frac{\Delta U}{U}\right\|$%	$\frac{\Delta U}{U}$ %
0 to 0.5s	-12.16	986.48	2.89	0.65
0.5s to 1s	-8.16	974.48	3.38	0.1
1s to 1.5s	-3.96	961.88	4	0.1
1.5s to 2s	+4.84	935.48	1	0.1
2s to 2.5s	+11.64	915.08	1.58	0.32

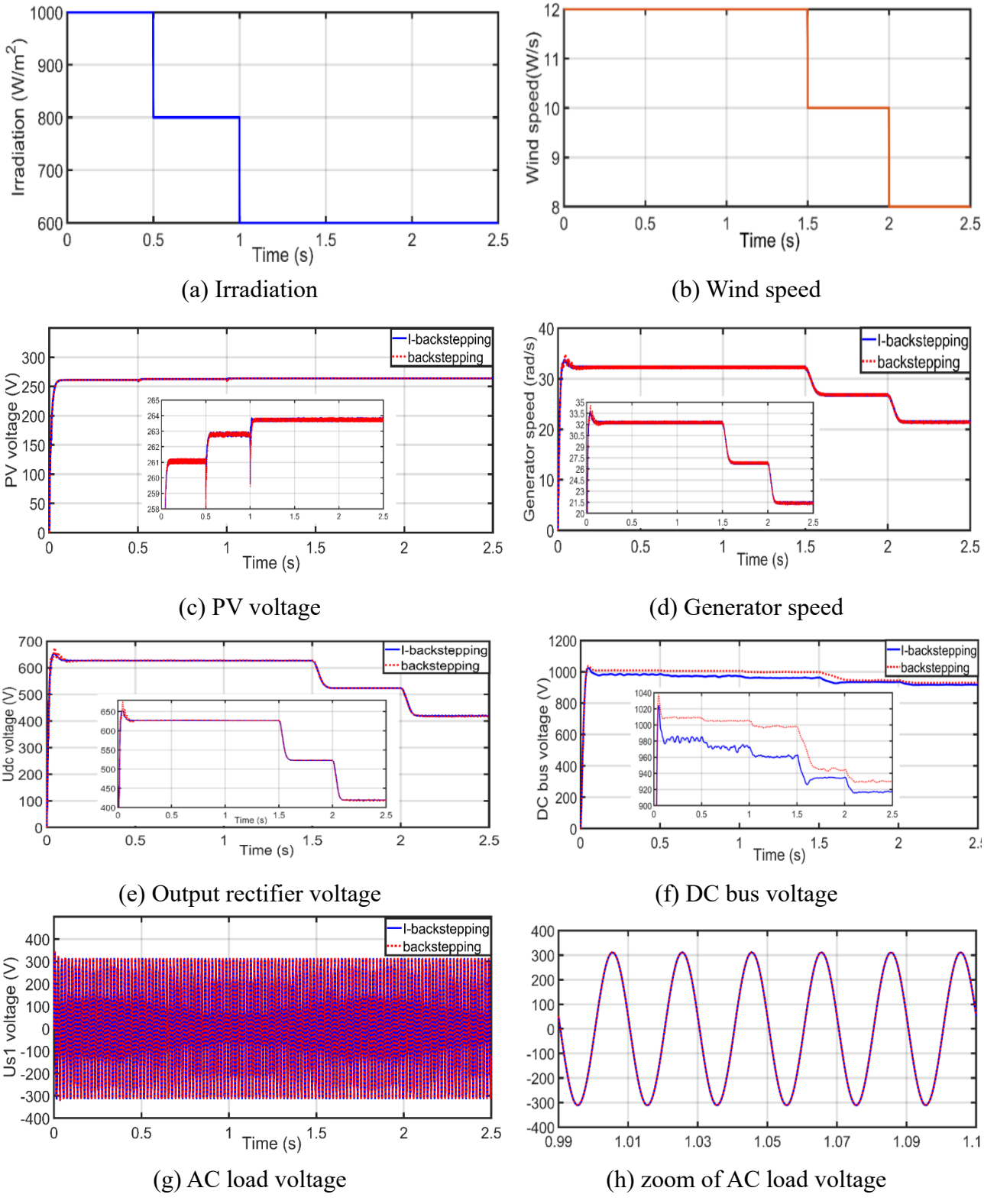

(a) Irradiation (b) Wind speed

(c) PV voltage (d) Generator speed

(e) Output rectifier voltage (f) DC bus voltage

(g) AC load voltage (h) zoom of AC load voltage

Figure 10. Simulation results for irradiance and wind speed changes.

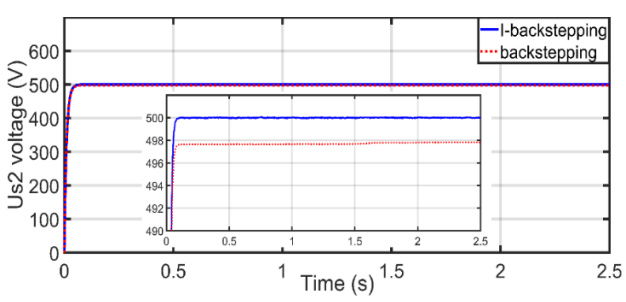

(i) DC load voltage

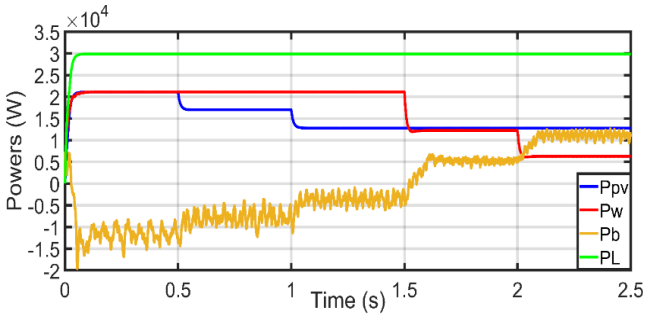

(j) Powers

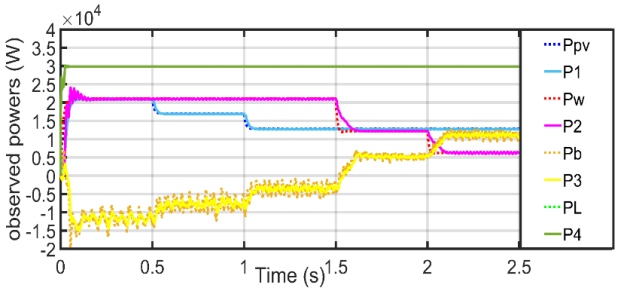

(k) Observed powers

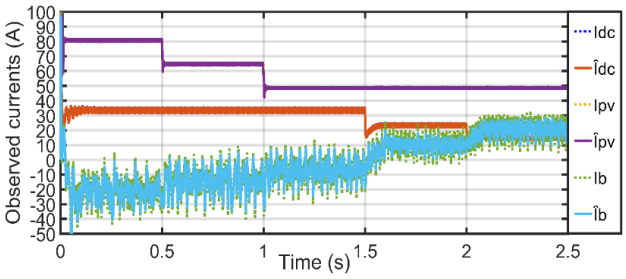

(l) Observed current

Figure 10. *Continued.*

Case 2. The performance of the controller varies with the load requirement.

It is commonly known that variations in load demand are common in power systems, particularly in the context of MG operation. Considering this, the change in the DC load demand power is considered in this example scenario to demonstrate the efficacy of the suggested controller (Figure 11(a)). In this case study, the PV source produced 21 kW of power, which was also equal to that of the wind power source because the irradiation was assumed to be constant at 1000 W/m2, the temperature was 25 °C, and the wind speed was 12 m/s. These conditions persisted until t = 2.5 s, as shown in Figure 11. Because the AC load value is constant at 10 Ω and the voltage at its terminals is regulated to an RMS value of 220V (Figure 11(f)), the AC load uses 4.84 kW of electrical power during the simulation. The DC load terminal voltage is controlled to 500V (Figure 11(h)), and the DC load requirement is 25 kW prior to the transient, that is, t = 0.5 s, as shown in Figure 11(j). Under the test conditions, the PV voltage is regulated at 261V (Figure 11(b)), the wind source speed is 32.2 rad/s (Figure 11(c)), and the output rectifier voltage is regulated at 628V (Figure 11(j)), which means that both the PV and the wind source operate at full power. For most signals, as shown in the previous test, it is difficult to discern a difference in performance between the conventional and the proposed control. For conventional backstepping control, the phase-transition regime shows a PIC in the output rectifier voltage, which is where the difference lies. Contrary to the conventional control, for the IB controller, the common DC bus voltage is also steadier and without errors compared to the desired value shown in Figure 11(e). Table 4 presents a comparison of the accuracy of the proposed control and traditional control, following the same methodology as in the previous test. This table unequivocally demonstrates that the DC bus voltage accuracy of the proposed control is higher than that of the conventional control. When the proposed command is used, the DC output voltage fluctuates slightly around the desired value. However, when the standard command was used, the deviations were larger, as shown in Figure 11(h).

Furthermore, simulations for traditional control were performed for comparison to confirm the ability of the proposed method to reject disturbances. Here, the load variation of the resistance was considered, specifically for the DC load change profile, as shown in Figure 11(a). Figure 11(h) shows that the proposed controller improves the closed-loop system's ability to reject disturbances.

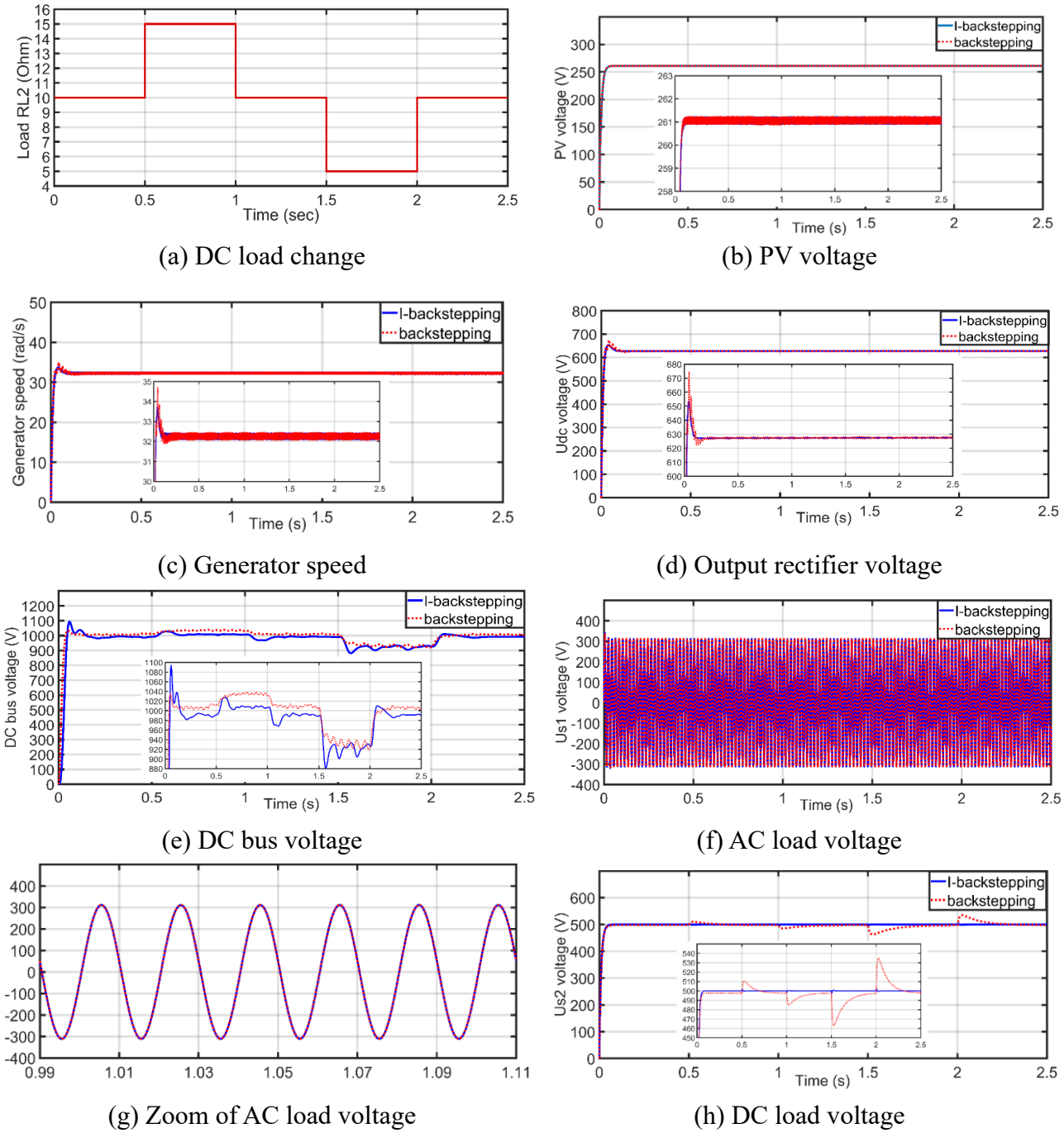

(a) DC load change (b) PV voltage

(c) Generator speed (d) Output rectifier voltage

(e) DC bus voltage (f) AC load voltage

(g) Zoom of AC load voltage (h) DC load voltage

Figure 11. Simulation results for DC load changes.

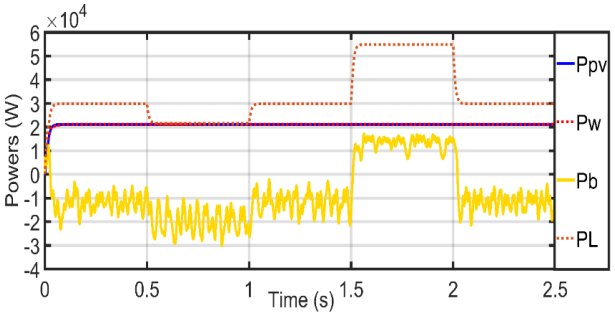

(i) Powers

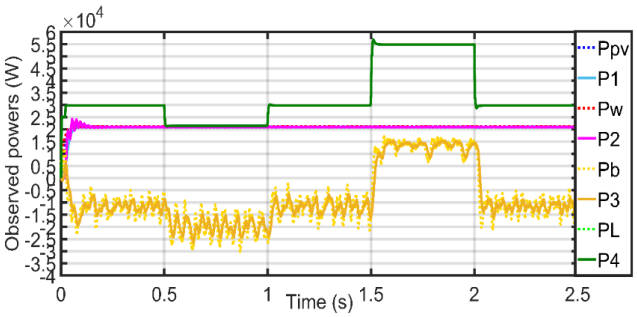

(j) Observed powers

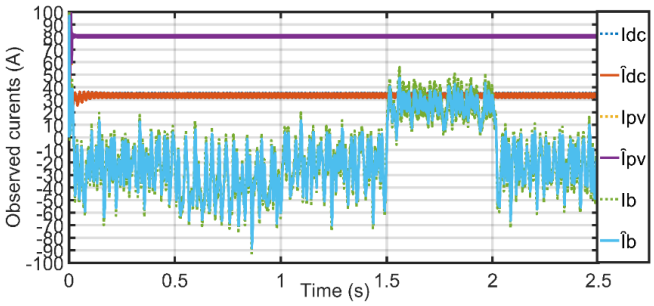

(k) Observed currents

Figure 11. *Continued.*

Table 4. DC bus voltage accuracy for DC load change.

Time (s)	P_b (kW)	$U_{Bus-ref}$ (V)	Conventional control [66]	Proposed control
			$\frac{\Delta U}{U}$ %	$\frac{\Delta U}{U}$ %
0 to 0.5s	-12.16	986.48	2.4	0.4
0.5s to 1s	-20.49	1011.47	2.86	0.29
1s to 1.5s	-12.16	986.48	2.4	0.4
1.5s to 2s	+12.84	911.48	2	0.98
2s to 2.5s	-12.16	986.48	2.4	0.4

To further substantiate the effectiveness of the proposed IB controller, its performance is benchmarked against other control strategies reported in the literature, including SMC [67], PI-based voltage regulation [68], adaptive backstepping [69], and FLC [70]. The comparison focuses on three critical performance indices—percentage overshoot, settling time of the DC bus voltage, and the total harmonic distortion (THD) of the output voltage—under identical test conditions. As summarized in Table 5, the proposed IB approach consistently outperforms the benchmark methods, achieving the lowest overshoot (0.31%), the fastest settling time (0.01 s), and a significantly reduced THD (1.8%). In contrast, PI and Sliding Mode controllers exhibit higher distortion levels, with PI reaching THD values as high as 12.7% in certain test intervals, while SMC maintains THD in the range of 1.2%–4.7%. Adaptive backstepping and FLC also show moderate improvements but remain inferior to the proposed approach in both dynamic and harmonic performance. These results confirm that the IB controller not

only enhances transient response robustness but also delivers cleaner power quality by suppressing harmonic distortion more effectively than existing control methods.

Table 5. Comparative performance of the proposed controller with recent works in the literature.

Reference	Method	Overshoot (%)	Settling Time (s)	SSE (V)	THD (%)	Remarks
[66]	Conventional Backstepping	0.82	0.20	5.2	3.5	Baseline method, slower and less robust
[67]	Sliding Mode Control	0.65	0.16	3.5	2.4	Robust but higher chattering
[68]	PI Control	1.32	0.23	4.8	3.1	Slow and higher steady-state error
[69]	Adaptive Backstepping	0.54	0.12	2.1	2.0	Sensitive to parameter variations
[70]	FLC	0.48	0.15	1.9	2.6	Requires extensive tuning
Proposed	IB + Observers	**0.31**	**0.01**	**0.8**	**1.8**	Fastest response, most accurate, disturbance rejection

For completeness and transparency, we note that all benchmark controllers (SMC [67], PI Control [68], adaptive backstepping [69], and FLC [70]) were implemented exactly as presented in their respective publications, with detailed formulations available in the cited works. To ensure fairness in comparison, identical system parameters—including PV/wind/battery ratings, DC bus nominal voltage (1000 V), switching frequency (5 kHz), and load variation profiles—were applied across all cases. Performance indices such as percentage overshoot, settling time, steady-state error, and THD (%) were uniformly measured. This ensures that the comparative study is both rigorous and directly aligned with prior literature while avoiding redundancy.

Now, let us examine the microgrid power balance during the simulation. Between 0 and 0.5 s, the combined power output of the sources is 42 kW, of which 25 kW is used by the DC load, 4.84 kW is required by the AC load and 12.16 kW of the excess power is routed to the battery for storage (Figure 11(i)). Between 0.5 and 1 s, the total power generated by both sources remains at 42 kW, the power consumption of the DC load drops to 16.666 kW, and the AC load's power demand stays at 4.84 kW. The battery stores the 20.49 kW of extra power. The load recovers to 10 Ohm in the interval of 1 to 1.5 s, and the numerical power values are the same as they were in the interval of 0 to 0.5 s. Between 1.5 and 2 s, the total power produced remains at 42 kW, the DC load power rises to 50 kW, the AC load power requirement stays at 4.84 kW, and the battery supplies a 12.84 kW power deficit. The DC load recovers to its nominal value in the interval 2s to 2.5s, and the power quantity involved are the same as those in the intervals 0 to 0.5 and 1s to 1.5s. It can be noted that there is nearly no difference between the actual and observed values of currents and powers (Figure 11(j) and (k)). As noted in the previous test, this observation was recorded and it was demonstrated that the implemented observers provided a higher quality image of the observed signals, as evidenced by the speed and small error between the observed signal and its real signal.

7. Conclusions

This study introduces an integral backstepping controller to ensure the dynamic stability and sustainability of DC microgrids. The proposed controller is developed by analyzing power variation rates associated with system states and applying Lyapunov energy theory, which guarantees robust dynamic stabilization. Unlike conventional backstepping control, the IB approach is specifically designed to achieve finite-time stability, thereby improving control accuracy. Comprehensive simulations under diverse operating conditions validate the theoretical findings. The results confirm that the proposed controller effectively maintains power balance among the PV system, permanent magnet synchronous generator, and battery energy storage system, while ensuring that the DC bus voltage remains within the desired range.

The key conclusions of this work are as follows:

- The controller successfully regulates the common DC bus voltage, optimizes power output from PV and wind sources, and stabilizes voltage levels at DC and AC load terminals, even under challenging conditions such as sudden load changes and power fluctuations.
- The proposed system effectively observes and monitors currents and power requirements with high accuracy, ensuring reliable system performance.
- Simulation results demonstrate that the proposed control strategy outperforms traditional methods, delivering significantly improved accuracy and dynamic performance.

This study highlights the potential of the IB controller as an efficient and reliable solution for managing the complexities of DC microgrids. The main advantages of the proposed control scheme include: (i) robustness against load uncertainties and disturbances, (ii) improved dynamic performance compared to traditional backstepping, and (iii) reduced sensor requirements due to observer-based estimation. Nonetheless, certain limitations should be acknowledged. The design requires careful gain tuning, which may increase implementation complexity.

Building upon this research, future efforts will focus on developing a laboratory-scale microgrid testbed to experimentally validate the proposed controller, investigating its performance under hardware non-idealities, communication delays, and real-time uncertainties.

Author contributions

Hassan Abouobaida: Performed conceptualization, methodology, software development, and writing the original draft; Safeer Ullah: Responsible for conceptualization, data curation, supervision and contributed to writing and reviewing the manuscript; Muhammad Zeeshan Babar: Carried out investigation, provided resources, and ensured validation of the study; Sultan Alghamdi: Contributed to visualization, formal analysis, and writing – review and editing; Ahmed S. Alsafran: Managed project administration, secured funding for the research, and contributed to writing – review and editing. All authors have read and approved the final manuscript.

Use of Generative-AI tools declaration

The authors declare they have not used artificial intelligence (AI) tools in the creation of this article.

Acknowledgments

This work was supported in part by the Deanship of Scientific Research at King Faisal University, Saudi Arabia, under Grant No. KFU253495; and in part by Heriot-Watt University, Edinburgh EH14 4AS, United Kingdom. The research was also supported in part by a UKRI grant (ERC-RES922610).

Conflict of interest

The authors declare no conflict of interest related to this work.

References

1. Y. S. Mohammed, M. W. Mustafa, N. Bashir, I. S. Ibrahem, Existing and recommended renewable and sustainable energy development in Nigeria based on autonomous energy and microgrid technologies, *Renew. Sustain. Energy Rev.*, **75** (2017), 820–838. https://doi.org/10.1016/j.rser.2016.11.062
2. A. Muhtadi, D. Pandit, N. Nguyen, J. Mitra, Distributed energy resource-based microgrid: Review of architecture, control, and reliability, *IEEE Trans. Ind. Appl.*, **57** (2021), 2223–2235. https://doi.org/10.1109/TIA.2021.3065329
3. A. A. Kumar, N. A. Prabha, A comprehensive review of DC microgrid in market segments and control technique, *Heliyon*, **8** (2022), e11694. https://doi.org/10.1016/j.heliyon.2022.e11694
4. C. A. Nallolla, V. P, D. Chittathuru, S. Padmanaban, Multi-objective optimization algorithms for a hybrid AC/DC microgrid using RES: A comprehensive review, *Electronics*, **12** (2023), 1062. https://doi.org/10.3390/electronics12041062
5. N. Khosravi, R. Baghbanzadeh, A. Oubelaid, M. Tostado-Véliz, M. Bajaj, Z. Hekss, et al., A novel control approach to improve the stability of hybrid AC/DC microgrids, *Appl. Energy*, **344** (2023), 121261. https://doi.org/10.1016/j.apenergy.2023.121261
6. D. Jain, D. Saxena, Comprehensive review on control schemes and stability investigation of hybrid AC-DC microgrid, *Electr. Power Syst. Res.*, **218** (2023), 109182. https://doi.org/10.1016/j.epsr.2023.109182
7. F. Dastgeer, H. E. Gelani, H. M. Anees, Z. J. Paracha, A. Kalam, Analyses of efficiency/energy-savings of DC power distribution systems/microgrids: Past, present and future, *Int. J. Electr. Power Energy Syst.*, **104** (2019), 89–100. https://doi.org/10.1016/j.ijepes.2018.06.057
8. M. Hasan, Z. Mifta, N. A. Salsabil, S. J. Papiya, M. Hossain, P. Roy, et al., A critical review on control mechanisms, supporting measures, and monitoring systems of microgrids considering large scale integration of renewable energy sources, *Energy Rep.*, **10** (2023), 4582–4603. https://doi.org/10.1016/j.egyr.2023.11.025
9. V. F. Pires, A. Pires A. Cordeiro, DC microgrids: Benefits, architectures, perspectives and challenges, *Energies*, **16** (2023), 1217. https://doi.org/10.3390/en16031217
10. L. R. Amjith, B. Bavanish, A review on biomass and wind as renewable energy for sustainable environment, *Chemosphere*, **293** (2022), 133579. https://doi.org/10.1016/j.chemosphere.2022.133579

11. M. Kiehbadroudinezhad, H. Hosseinzadeh-Bandbafha, M. A. Rosen, V. K. Gupta, W. Peng, M. Tabatabaei, et al., The role of energy security and resilience in the sustainability of green microgrids: Paving the way to sustainable and clean production, *Sustain. Energy Technol. Assess*., **60** (2023), 103485. https://doi.org/10.1016/j.seta.2023.103485
12. C. R. Kumar. J, M. A. Majid, Renewable energy for sustainable development in India: Current status, future prospects, challenges, employment, and investment opportunities, *Energ. Sustain. Soc.*, **10** (2020), 2. https://doi.org/10.1186/s13705-019-0232-1
13. E. Naderi, S. J. SeyedShenava, H. Shayeghi, High gain DC/DC converter implemented with MPPT algorithm for DC microgrid system, *J. Oper. Autom. Power Eng.*, **11** (2023), 213–222. https://doi.org/10.22098/joape.2023.10270.1731
14. A. K. Pandey, V. Singh, S. Jain, Chapter eleven - Study and comparative analysis of perturb and observe (P&O) and fuzzy logic based PV-MPPT algorithms, In: *Applications of AI and IOT in renewable energy,* Academic Press, 2022, 193–209. https://doi.org/10.1016/B978-0-323-91699-8.00011-5
15. M. A. B. Siddique, A. Asad, R. M. Asif, A. U. Rehman, M. T. Sadiq, I. Ullah, Implementation of incremental conductance MPPT algorithm with integral regulator by using boost converter in grid-connected PV array, *IETE J. Res.*, **69** (2023), 3822–3835. https://doi.org/10.1080/03772063.2021.1920481
16. P. Bhatia, S. Mittal, S. Raizada, V. Verma, Hybrid ANN based incremental conductance MPPT-current control algorithm for constant power generation of PV fed DC microgrid, In: *2020 IEEE First international conference on smart technologies for power, energy and control (STPEC)*, Nagpu: IEEE, 2020, 1–7. https://doi.org/10.1109/STPEC49749.2020.9297751
17. F. Yahiaoui, F. Chabour, O. Guenounou, M. Bajaj, S. S. H. Bukhari, M. S. Nazir, et al., An experimental testing of optimized fuzzy logic-based MPPT for a standalone PV system using genetic algorithms, *Math. Probl. Eng.*, 2023. https://doi.org/10.1155/2023/4176997
18. V. Subramanian, V. Indragandhi, R. Kuppusamy, Y. Teekaraman, Modeling and analysis of PV system with fuzzy logic MPPT technique for a DC microgrid under variable atmospheric conditions, *Electronics*, **10** (2021), 2541. https://doi.org/10.3390/electronics10202541
19. P. Bahrani, N. Jain, Performance analysis of P&O and FLC method of MPPT for PV module based on five-parameter model, In: *Proceedings of international conference on computational intelligence and emerging power system*, Singapore: Springer, 2021, 357–369. https://doi.org/10.1007/978-981-16-4103-9_30
20. S. S. Pradhan, R. Pradhan, B. Subudhi, A hybrid incremental conductance and sliding mode controller for a PV microgrid system, *Int. J. Intell. Syst. Des. Comput.*, **3** (2020), 145–160. https://dx.doi.org/10.1504/IJISDC.2020.115170
21. D. Žigman, S. Tvorić, M. Lonić, Comparative PSO optimisation of microgrid management models in Island operation to minimise cost, *Energies*, **17** (2024), 3901. https://doi.org/10.3390/en17163901
22. R. Wazirali, E. Yaghoubi, M. S. S. Abujazar, R. Ahmad, A. H. Vakili, State-of-the-art review on energy and load forecasting in microgrids using artificial neural networks, machine learning, and deep learning techniques, *Electr. Power Syst. Res.*, **225** (2023), 109792. https://doi.org/10.1016/j.epsr.2023.109792

23. Z. H. A. Al-Tameemi, T. T. Lie, G. Foo, F. Blaabjerg, Optimal coordinated control of DC microgrid based on hybrid PSO–GWO algorithm, *Electricity*, **3** (2022), 346–364. https://doi.org/10.3390/electricity3030019
24. R. K. Rojin, M. M. Linda, Hybrid microgrid based on PID controller with the modified particle swarm optimization, *Intell. Autom. Soft Comput.*, **33** (2022), 245–258. https://doi.org/10.32604/iasc.2022.021834
25. S. Ullah, A. Mehmood, Q. Khan, S. Rehman, J. Iqbal. Robust integral sliding mode control design for stability enhancement of under-actuated quadcopter, *Int. J. Control Autom. Syst.*, **18** (2020), 1671–1678. https://doi.org/10.1007/s12555-019-0302-3
26. H. M. M. Adil, H. A. Khan, Renewable energy integration using supertwisted integral backstepping control of DC microgrid, In: *2024 IEEE Power & energy society innovative smart grid technologies conference (ISGT)*, Washington: IEEE, 2024, 1–5. https://doi.org/10.1109/ISGT59692.2024.10454232
27. Q. Zhang, X. Zhuang, Y. Liu, C. Wang, H. Guo, A novel control strategy for mode seamless switching of PV converter in DC microgrid based on double integral sliding mode control, *ISA Trans.*, **100** (2020), 469–480. https://doi.org/10.1016/j.isatra.2019.12.013
28. S. Ullah, Q. Khan, A. Mehmood, A. I. Bhatti, Robust backstepping sliding mode control design for a class of underactuated electro–mechanical nonlinear systems, *J. Electr. Eng. Technol*., **15** (2020), 1821–1828. https://doi.org/10.1007/s42835-020-00436-3
29. M. T. Vu, D. H. Pham, V. T. Nguyen, Q. T. Do, A. K. Alanazi, T. H. Nguyen, Adaptive nonlinear integral-backstepping control for frequency stabilization in cyber-physical shipboard microgrids using double deep Q-learning, *Eng. Appl. Artif. Intell.*, **160** (2025), 111943. https://doi.org/10.1016/j.engappai.2025.111943
30. S. Wang, Q. Cheng, B. Shangguan, J. Ma, N. Jiao, T. Liu, Accurate and continuous reactive power control of three-terminal hybrid DC transmission system, *IEEE Trans. Power Del.*, **40** (2025), 30–40. https://doi.org/10.1109/TPWRD.2024.3480270
31. M. Sahani, B. Biswal, E. N. Prasad, P. K. Dash, S. K. Panda, An adaptive integral backstepping SMC and robust functional expanded multikernel BLS based MPPT control in PV-battery DC microgrid system, *IEEE Trans. Power Electron*., **39** (2024), 2966–2979. https://doi.org/10.1109/TPEL.2023.3332641
32. J. Lu, X. Zhang, X. Hou, P. Wang, Generalized extended state observer-based distributed attack-resilient control for DC microgrids, *IEEE Trans. Sustain. Energy*, **13** (2022), 1469–1480. https://doi.org/10.1109/TSTE.2022.3162757
33. V. S. Saravi, H. Sakhaei, M. Kalantar, A. Anvari-Moghaddam, A novel power management strategy based on combination of 3D droop control and EKF in DC microgrids, *IET Renew. Power Gener.*, **15** (2021), 2540–2555. https://doi.org/10.1049/rpg2.12187
34. N. Vafamand, M. M. Arefi, M. Shafie-Khah, J. P. S. Catalão, Adaptive optimal control of faulty nonlinear DC microgrids with constant power loads: Dual-extended Kalman filter approach, *IEEE Trans. Ind. Appl.*, **59** (2023), 513–522. https://doi.org/10.1109/TIA.2022.3206169
35. R. Errouissi, A. Al-Durra, Extended high-gain observer-based DC-link voltage regulation in dual-stage grid-tied PV system under balanced and unbalanced voltages, *IET Renew. Power Gener.*, **14** (2020), 2037–2046. https://doi.org/10.1049/iet-rpg.2019.0973

36. A. T. Azar, A. M. Abed, F. A. Abdulmajeed, I. A. Hameed, N. A. Kamal, A. J. M. Jawad, et al., A new nonlinear controller for the maximum power point tracking of photovoltaic systems in micro grid applications based on modified anti-disturbance compensation, *Sustainability*, **14** (2022), 10511. https://doi.org/10.3390/su141710511
37. R. Sharma, A. Almelkar, K. Baghel, S. Syed, K. Sonam, Extended high gain observer based control design for buck-boost converters, In: *2019 6th International conference on control, decision and information technologies (CoDIT)*, 2019, 669–674. https://doi.org/10.1109/CoDIT.2019.8820349
38. Y. Liu, Y. Wang, S. Chen, J. Zhang, A novel hybrid neural Lyapunov method with low conservatism for power system Domain of attraction estimation, *IEEE Trans. Ind. Inform.*, **21** (2025), 5580–5591. https://doi.org/10.1109/TII.2025.3556059
39. M. Li, Y. Chen, M. Zhang, H. Song, Adaptive NN observer-based synthesize strategy for connected nonlinear system, *IEEE Trans. Autom. Sci. Eng.*, **22** (2025), 14798–14807. https://doi.org/10.1109/TASE.2025.3564331
40. M. H. Sabzalian, K. A. Alattas, F. F. M. El-Sousy, A. Mohammadzadeh, S. Mobayen, M. T. Vu, et al., A neural controller for induction motors: Fractional-order stability analysis and online learning algorithm, *Mathematics*, **10** (2022), 1003. https://doi.org/10.3390/math10061003
41. S. Y. Rahme, S. Islam, S. M. Amrr, A. Iqbal, I. Khan, M. Marzband, Adaptive sliding mode control for instability compensation in DC microgrids due to EV charging infrastructure, *Sustain. Energy Grids Netw.*, **35** (2023), 101119. https://doi.org/10.1016/j.segan.2023.101119
42. H. Pan, X. Feng, F. Li, J. Yang, Energy coordinated control of DC microgrid integrated incorporating PV, energy storage and EV charging, *Appl. Energy*, **342** (2023), 121155. https://doi.org/10.1016/j.apenergy.2023.121155
43. B. Modu, M. P. Abdullah, M. A. Sanusi, M. F. Hamza, DC-based microgrid: Topologies, control schemes, and implementations, *Alex. Eng. J.*, **70** (2023), 61–92. https://doi.org/10.1016/j.aej.2023.02.021
44. S. Srinivasan, R. Tiwari, M. Krishnamoorthy, M. P. Lalitha, K. K. Raj, Neural network based MPPT control with reconfigured quadratic boost converter for fuel cell application, *Int. J. Hydrogen Energy*, **46** (2021), 6709–6719. https://doi.org/10.1016/j.ijhydene.2020.11.121
45. S. Ozdemir, N. Altin, I. Sefa, Fuzzy logic-based MPPT controller for high conversion ratio quadratic boost converter, *Int. J. Hydrogen Energy*, **42** (2017), 17748–17759. https://doi.org/10.1016/j.ijhydene.2017.02.191
46. H. Armghan, M. Yang, M. Q. Wang, N. Ali, A. Armghan, Nonlinear integral backstepping based control of a DC microgrid with renewable generation and energy storage systems, *Int. J. Electr. Power Energy Syst.*, **117** (2020), 105613. https://doi.org/10.1016/j.ijepes.2019.105613
47. T. K. Roy, S. K. Ghosh, S. Saha, Stability enhancement of battery energy storage and renewable energy-based hybrid AC/DC microgrids using terminal sliding mode backstepping control approaches, *ISA Trans.*, **142** (2023), 40–56. https://doi.org/10.1016/j.isatra.2023.07.014
48. E. N. V. D. V. Prasad, M. Sahani, P. K. Dash, A new adaptive integral back stepping fractional order sliding mode control approach for PV and wind with battery system based DC microgrid, *Sustain. Energy Technol. Assess.*, **52** (2022), 102261. https://doi.org/10.1016/j.seta.2022.102261
49. B. Li, T. Huang, Z. Kong, L. Chen, J. Yang, S. Sun, Discrete control for state of charge balance in DC microgrids considering the disturbance of photovoltaics, *Int. J. Electr. Power Energy Syst.*, **157** (2024), 109879. https://doi.org/10.1016/j.ijepes.2024.109879

50. N. Ali, X. Shen, H. Armghan, Y. Du, Hierarchical control combined with higher order sliding mode control for integrating wind/tidal/battery/hydrogen powered DC offshore microgrid, *J. Energy Storage*, **82** (2024), 110521. https://doi.org/10.1016/j.est.2024.110521
51. V. Vásquez, L. M. Ortega, D. Romero, R. Ortega, O. Carranza, J. J. Rodríguez, Comparison of methods for controller design of single-phase inverter operating in island mode in a microgrid: Review, *Renew. Sustain. Energy Rev.*, **76** (2017), 256–267. https://doi.org/10.1016/j.rser.2017.03.060
52. M. Azab, A finite control set model predictive control scheme for single-phase grid-connected inverters, *Renew. Sustain. Energy Rev.*, **135** (2021), 110131. https://doi.org/10.1016/j.rser.2020.110131
53. Z. Wang, S. Li, J. Wang, Q. Li, Robust control for disturbed buck converters based on two GPI observers, *Control Eng. Pract.*, **66** (2017), 13–22. https://doi.org/10.1016/j.conengprac.2017.06.001
54. J. Lu, M. Savaghebi, Y. Guan, J. C. Vasquez, A. M. Y. M. Ghias, J. M. Guerrero, A reduced-order enhanced state observer control of DC-DC buck converter, *IEEE Access*, **6** (2018), 56184–56191. https://doi.org/10.1109/ACCESS.2018.2872156
55. Z. Wang, T. Guo, X. Wang, S. Li, GPI observer-based composite current-constrained control approach for DC-DC buck converters, *J. Eng.*, 2019 (2019), 581–586. https://doi.org/10.1049/joe.2018.9386
56. O. Boutebba, S. Semcheddine, F. Krim, B. Talbi, A. Reatti, F. Corti, Robust non-linear controller design for DC-DC buck converter via modified back-stepping methodology, *Elektron. Elektrotech.*, **28** (2022), 4–11. https://doi.org/10.5755/j02.eie.31487
57. D. Yu, W. Zhang, Z. Chu, H. Zhang, Z. Wang, An optimized synchronous approach to DC/DC droop backstepping control considering voltage compensation in DC microgrids, *Electr. Power Syst. Res*., **228** (2024), 110014. https://doi.org/10.1016/j.epsr.2023.110014
58. B. S. V. Sai, S. A. Khadtare, D. Chatterjee, An improved weather adaptable P&O MPPT technique under varying irradiation condition, *ISA Trans.*, **140** (2023), 438–458. https://doi.org/10.1016/j.isatra.2023.05.025
59. M. J. Khan, An AIAPO MPPT controller based real time adaptive maximum power point tracking technique for wind turbine system, *ISA Trans.*, **123** (2022), 492–504. https://doi.org/10.1016/j.isatra.2021.06.008
60. I. Toumi, A. Boulmaiz, B. Meghni, O. Hachana, Robust variable step P&O algorithm-based MPPT for PMSG wind generation system using estimated wind speed compensation technique, *Sustain. Energy Technol. Assess.*, **60** (2023), 103420. https://doi.org/10.1016/j.seta.2023.103420
61. M. Rahimi, Modeling, control, and stability analysis of grid-connected PMSG-based wind turbine assisted with diode rectifier and boost converter, *Int. J. Electr. Power Energy Syst.*, **93** (2017), 84–96. https://doi.org/10.1016/j.ijepes.2017.05.019
62. M. A. Hassan, Y. He, Constant power load stabilization in DC microgrid systems using passivity-based control with nonlinear disturbance observer*, IEEE Access*, **8** (2020), 92393–92406. https://doi.org/10.1109/ACCESS.2020.2992780
63. X. Li, L. Guo, S. Zhang, C. Wang, Y. W. Li, A. Chen, Observer-based DC voltage droop and current feed-forward control of a DC microgrid, *IEEE Trans. Smart Grid*, **9** (2018), 5207–5216. https://doi.org/10.1109/TSG.2017.2684178

64. J. Mohammadi, F. B. Ajaei, Improved mode-adaptive droop control strategy for the DC microgrid, *IEEE Access*, **7** (2019), 86421–86435. https://doi.org/10.1109/ACCESS.2019.2924994
65. J. Wang, S. Li, J. Yang, B. Wu, Q. Li, Extended state observer-based sliding mode control for PWM-based DC-DC buck power converter systems with mismatched disturbances, *IET Control Theory Appl.*, **9** (2015), 579–586. https://doi.org/10.1049/iet-cta.2014.0220
66. M. El Azzaoui, H. Mahmoudi, K. Boudaraia, Backstepping control of wind and photovoltaic hybrid renewable energy system, *Int. J. Power Electron. Drive Syst.*, **7** (2016), 677–686.
67. R. Benadli, M. Bjaoui, B. Khiari, A. Sellami, Sliding mode control of hybrid renewable energy system operating in grid connected and stand-alone mode, *Power Electron. Drives*, **6** (2021), 144–166. https://doi.org/10.2478/pead-2021-0009
68. R. Benadli, B. Khiari, B. Khiari, Control and simulation of a standalone photovoltaic-wind with a fuel cell and battery storage, *J. Electr. Eng.*, **20** (2021).
69. T. K. Roy, M. A. Mahmud, A. M. T. Oo, M. E. Haque, K. M. Muttaqi, N. Mendis, Nonlinear adaptive backstepping controller design for islanded DC microgrids, *IEEE Trans. Ind. Appl.*, **54** (2018), 2857–2873. https://doi.org/10.1109/TIA.2018.2800680
70. N. Alfred, V. Guntreddi, A. N. Shuaibu, M. S. Bakare, A fuzzy logic based energy management model for solar PV-wind standalone with battery storage system, *Sci. Rep.*, **15** (2025), 24660. https://doi.org/10.1038/s41598-025-09662-z

AIMS Press